applied system innovation

MDPI

Article

Hydrogen-Efficient Operation of a PEMFC-Powered Induction Motor Drive via Dhole-Inspired Optimization and a Neural Network Controller

Mahmoud M. Elkholy [1,2], A. El-Sayed [3], Hossam Ashraf [4,5], Mohammed Jufaili [1,*] and M. Abdelateef Mostafa [2]

1 Electrical Engineering and Computer Science Department, College of Engineering, A'Sharqiyah University, P.O. Box 42, Ibra 400, Oman; mahmoud.elkhouli@asu.edu.om
2 Electrical Power and Machines Engineering Department, Faculty of Engineering, Zagazig University, Zagazig 44511, Egypt; mabdellatef@zu.edu.eg
3 Electrical Engineering Department, Faculty of Engineering, Damanhour University, Damanhour 22511, Egypt; ahmed.metwally@eng.dmu.edu.eg
4 Department of Electrical Engineering and Information Systems, The University of Tokyo, Tokyo 113-8656, Japan; hossam-ashraf@g.ecc.u-tokyo.ac.jp
5 Electrical Engineering Department, Faculty of Engineering and FabLab in the Centre for Emerging Learning Technologies (CELT), The British University in Egypt (BUE), Cairo 11837, Egypt
* Correspondence: mohammed.aljufaili@asu.edu.om

Abstract

This paper presents an energy-efficient operating strategy for a three-phase induction motor drive powered by a proton exchange membrane fuel cell (PEMFC). The proposed approach minimizes hydrogen consumption and improves motor efficiency over a wide operating range by continuously regulating the motor terminal voltage according to the load demand. The optimal reference voltage corresponding to each load torque is determined using the dholes-inspired optimization algorithm (DIOA), a recent swarm-based optimization technique. The DIOA is also employed to determine the optimal parameters of a proportional–integral (PI) controller, enabling accurate and rapid tracking of the reference voltage. To evaluate the effectiveness of the proposed optimizer, its performance is compared with the well-known particle swarm optimization (PSO) algorithm. The reference voltages obtained using the DIOA and PSO differ by less than 1.1%, their hydrogen consumptions differ by less than 0.02%, and a direct voltage sweep confirms the optimum. The dynamic performance is investigated using both an optimally tuned PI controller and a neural network controller (NNC). Simulation results show that the NNC provides faster settling, lower transient deviations, and improved dynamic performance compared with the PI controller. Steady-state results indicate that hydrogen savings are strongly dependent on motor loading. At a load torque of 0.5 N·m (5% of full load), hydrogen consumption is reduced from 1.999121 slpm to 0.706726 slpm, representing a saving of 64.65%. At a load torque of 2 N·m (20% of full load), the hydrogen saving reaches 24.17%. As the load approaches its rated value, the motor operates near its maximum efficiency and rated voltage.

Keywords: PEMFC; induction motor; dholes-inspired optimization algorithm; particle swarm optimization; Neural Network Controller

Check for updates

Academic Editor: Wu Deng

Received: 15 September 2026
Revised: 20 October 2026
Accepted: 26 October 2026
Published: 29 October 2026

Copyright: © 2026 by the authors. Published by MDPI on behalf of the International Institute of Knowledge Innovation and Invention. Licensee MDPI, Basel, Switzerland. This article is an open access article distributed under the terms and conditions of the Creative Commons Attribution (CC BY) license.

1. Introduction

Currently, climate change and the continuous increase in greenhouse gas emissions have made energy system decarbonization a global priority [1]. Hence, renewable

energy sources (RESs), such as photovoltaic and wind power, play a central role in such transition. However, their variability and intermittency limit reliable large-scale integration into power systems [2]. Consequently, hydrogen has emerged as a promising clean energy carrier. In addition, it can be produced using RES-powered electrolysis, stored for later use, and utilized across multiple sectors to support decarbonization [3]. Hydrogen can also be converted back into electricity using fuel cells, where hydrogen reacts electrochemically with oxygen to generate electrical power while producing only water as a by-product [4].

In this context, proton exchange membrane fuel cells (PEMFCs) are among the most promising fuel cell technologies [5]. Particularly, they offer high energy conversion efficiency along with low operating temperatures around 60–80 °C [6]. Additionally, PEMFCs provide high power density, short startup time, and fast dynamic response to load variations [7]. Accordingly, they offer a suitable energy alternative for transportation and distributed power applications. Furthermore, PEMFC technology has been widely adopted in electric drive systems due to its efficiency, compactness, and zero-emission operation [8]. Therefore, PEMFCs are selected in this work as a promising technology for advanced energy conversion systems.

In this regard, PEMFCs are increasingly integrated with electric motor drive systems in practical energy applications. In such systems, the fuel cell converts hydrogen into electrical energy that supplies the electric propulsion system to produce mechanical motion [9]. The overall powertrain typically integrates the fuel cell stack, auxiliary energy storage devices, electric motors, and power electronic converters into a coordinated drive system [10]. Moreover, power electronic converters such as DC-DC converters and motor drive inverters play a crucial role in regulating voltage and controlling the motor speed and torque. These technologies have enabled the widespread use of AC motors in fuel-cell-powered transportation systems [11].

On the other hand, efficient system operation requires advanced control and energy management strategies to coordinate the interaction between the PEMFCs, power converters, and electric motor under varying operating conditions [12]. Thus, several control approaches have been proposed to regulate this interaction. For example, conventional techniques, such as proportional–integral (PI) controllers [13], are widely used to regulate the PEMFC current and maintain the DC-bus voltage stability through duty cycle control. In addition, advanced motor control methods such as field-oriented control (FOC) [14] and direct torque control (DTC) [15] have been extensively applied to improve torque tracking and the dynamic response of electric drives. However, these classical methods have several limitations. FOC requires accurate motor parameter estimation and coordinate transformations, making it sensitive to parameter variations and model uncertainties [16]. Similarly, DTC can produce high torque and current ripples and may suffer from variable switching frequency, which affects system efficiency and stability [17].

Moreover, these limitations become more critical since PEMFCs exhibit highly nonlinear electrochemical behavior and operate under varying conditions such as temperature, pressure, hydrogen flow rate, and load demand [18]. As a result, model-based techniques such as FOC and DTC may experience degraded performance when system parameters change or when operating conditions fluctuate. Consequently, researchers have increasingly explored intelligent control techniques, including fuzzy logic, artificial neural networks (ANNs), and hybrid AI-based controllers. Principally, such approaches can learn system behavior and adapt to nonlinear dynamics without requiring precise mathematical models [19]. In addition, energy management strategies (EMS) are often integrated not only to coordinate the interaction between different components in hybrid

PEMFC systems but also to improve overall efficiency and hydrogen utilization [20]. Therefore, advanced intelligent control approaches have emerged as promising solutions for improving the robustness and efficiency of PEMFC-based electric drive systems.

Accordingly, numerous studies have investigated different architectures, motor types, and control strategies for integrating fuel cells with electric motors. In this context, a comparative overview of representative studies reported in the literature is presented in Table 1. Specifically, it summarizes the main applications, system configurations, modeling approaches, and control techniques used in previous works.

As captured from Table 1, PEMFCs are the most widely used fuel cell technology in these systems due to their fast dynamic response and suitability for transportation and distributed generation applications. Moreover, most reported studies employ three-phase induction motors because of their robustness, reliability, and low cost. However, other machines such as permanent magnet synchronous motors (PMSMs), switched reluctance motors (SRMs), and synchronous motors have also been investigated.

Furthermore, the reviewed works typically use DC-DC converters combined with three-phase inverters to interface the fuel cell with the motor drive. In addition, the majority of studies rely on MATLAB/Simulink dynamic models to analyze system behavior and performance. In addition, various control techniques have been applied in the literature. These include vector control, MPPT methods, fuzzy logic controllers, ANN, ANFIS-based controllers, and metaheuristic-optimized PI controllers. Thus, some studies also investigate hybrid architectures, where the fuel cell is combined with supercapacitors or batteries to improve transient performance.

Table 1. Summary of representative studies on PEMFC-powered motor drive systems.

Ref.	Application	Fuel Cell Type	Motor Type	Converter Type	Main Model Type	Control Strategy	Hydrogen-Related Optimization (Approach)	Key Contribution
[21] (2018)	FC-powered induction motor drive for remote applications	PEMFC	3-phase induction motor	Boost DC-DC + 3-phase inverter	MAT-LAB/Simulink dynamic model	ANFIS-based MPPT + ANFIS inverter control	No	ANFIS-MPPT improves transient response and stability compared with conventional methods.
[22] (2021)	PEMFC powered induction motor drive	PEMFC	3-phase induction motor	Interleaved high step-up DC-DC converter + VSI	MAT-LAB/Simulink + experimental prototype	ANN-based MPPT + SVPWM	No	ANN-MPPT improves power extraction and converter efficiency.
[23] (2006)	Railway traction drive system	PEMFC	Induction traction motors	Voltage source inverter	Experimental traction system validation	Slip-frequency vector control	No	Demonstrates experimentally that PEMFC can supply inverter-driven induction traction motors and follow rapid load changes.
[24] (2014)	Renewable water pumping system	PEMFC (hybrid PV-FC)	3-phase induction motor (pump load)	DC-DC boost + PWM inverter	MAT-LAB/Simulink hybrid renewable system model	Fuzzy logic MPPT	No	Hybrid PV-PEMFC system supplying induction motor pump with fuzzy-MPPT for improved renewable power utilization.
[25] (2024)	FC–supercapacitor-powered induction motor drive	PEMFC + Supercapacitor	Open-end winding induction motor	Dual inverter configuration	MAT-LAB/Simulink dynamic drive model	FOC + energy management	Yes energy management	Hybrid FC–supercapacitor architecture improves drive efficiency and transient power support.
[26] (2025)	PEMFC-based electric vehicle	PEMFC	AC induction motor	DC-DC boost converter + battery interface	Experimental EV system analysis	Hydrogen flow regulation study	Yes fuel flow regulation, experimental	Experimental investigation of hydrogen flow influence on PEMFC efficiency and power output in EV applications.
[27] (2017)	Electric vehicle traction drive	PEMFC	3-phase induction motor	DC-DC boost converter + VSI	MAT-LAB/Simulink dynamic drive model	Vector control FOC	No	Demonstrates PEMFC-assisted vector-controlled induction motor drive for EV propulsion.
[28] (2022)	Hybrid renewable water pumping system	SOFC (hybrid PV-SOFC)	3-phase induction motor (pump load)	Boost DC-DC + inverter + battery interface	MAT-LAB/Simulink hybrid energy system model	Cuckoo search algorithm MPPT + PI control	No	CSA-based MPPT and PI tuning improve power extraction and maintain stable DC bus for motor-driven pumping system.

Table 1. *Cont.*

Ref.	Application	Fuel Cell Type	Motor Type	Converter Type	Main Model Type	Control Strategy	Hydrogen-Related Optimization (Approach)	Key Contribution
[29] (2024)	Distributed generation/induction motor drive system	SOFC	3-phase squirrel cage induction motor	DC-AC three-phase inverter	MATLAB/Simulink dynamic SOFC model	PWM inverter control	No	Dynamic modeling of SOFC with inverter supplying a three-phase induction motor and fault analysis of the drive system.
[30] (2024)	FC electric vehicle powertrain analysis	Alkaline fuel cell (AFC)	PMSM	DC-DC converter + traction inverter	MATLAB/Simulink vehicle powertrain model	Vehicle energy management strategy	Yes vehicle energy management	Comparative analysis of AFC-based electric vehicle performance and hydrogen consumption using a PMSM traction drive.
[31] (2021)	Stand-alone renewable energy system supplying motor load	PEMFC (hybrid PV-PEMFC)	PMSM	DC-DC boost + inverter	MATLAB/Simulink hybrid renewable system model	MPPT control for PV + energy management	No	Hybrid PV-PEMFC standalone system designed to supply a synchronous motor load with improved energy utilization.
[32] (2019)	PEMFC-powered switched reluctance motor drive	PEMFC	SRM	H-bridge converter	MATLAB/Simulink dynamic drive model	PI controller optimized by multi-objective dragonfly optimizer (MODA)	No	MODA optimizes converter switching angles and PI gains to improve torque ripple, torque/ampere ratio, and starting torque.
This Work	FC-powered induction motor drive with hydrogen consumption minimization	PEMFC	3-phase induction motor	DC-DC chopper + 3-phase inverter	MATLAB/Simulink nonlinear PEMFC-motor dynamic model	Metaheuristic-optimized PI vs. NARMA-L2 predictive neural controller	Yes drive voltage versus stack hydrogen flow, at each load s	Minimizes the stack hydrogen consumption by optimizing the DC-link voltage reference at each load torque (DIOA/PSO), with optimized PI and NARMA-L2 neural voltage control.

Despite the significant progress reported in the literature, several research gaps remain in PEMFC-powered motor drive systems. Firstly, most existing studies focus on improving power extraction, efficiency, or dynamic performance. Hydrogen-related optimization has been reported mainly at the energy-management level of hybrid fuel cell drives and vehicles [25,30], or as an experimental study of fuel flow regulation [26]. To the best of the authors' knowledge, none of the reviewed studies minimizes the hydrogen consumption of the stack by optimizing the motor terminal voltage of an induction motor drive at each load torque.

Reducing the flux of an induction motor at light load is a classical way to improve its efficiency. Loss-model controllers calculate the flux (or voltage) that minimizes the motor losses from the machine parameters, while search controllers adjust the flux or voltage online until the input power is minimal; both families are well established for induction motors, including scalar-controlled (V/f) drives [33–37]. These works minimize the losses of the motor, and possibly of the inverter, and do not include the fuel cell. In a PEMFC-fed drive the quantity to be minimized is the hydrogen flow, which also depends on the polarization curve of the stack and on the converter. Therefore, the optimal DC-link voltage is not necessarily the one that minimizes the motor losses alone.

In addition, the majority of reported works rely on classical control methods, such as PI control or vector control. Only limited studies investigate the comparison between conventional controllers and advanced intelligent controllers. Therefore, further research is required to develop advanced control strategies that explicitly minimize hydrogen consumption while maintaining the required motor performance.

Consequently, this paper investigates the optimal operation of a PEMFC-powered induction motor drive system with the objective of reducing hydrogen consumption while maintaining the required motor performance. Thus, the main contributions of this work are: (i) a stack-to-shaft formulation in which the hydrogen consumption of the PEMFC is minimized by optimizing, at each load torque, the DC-link voltage reference of a scalar-controlled induction-motor drive, and unlike classical loss-minimization controllers [33–37], the objective includes the operating point of the stack and the converter; (ii) a load-dependent reference-voltage map obtained offline with DIOA and compared with PSO, together with the DIOA-based tuning of the PI controller of the boost converter; (iii) a NARMA-L2 neural voltage controller compared with the optimized PI controller under a load step; and (iv) quantified hydrogen savings of 64.65% at 0.5 N·m and 24.17% at 2 N·m with respect to operation at the rated DC-link voltage (537 V). The drive uses scalar control: the inverter operates at a fixed frequency and modulation index (Figure 1), and the motor terminal voltage is adjusted through the DC-link voltage. Only the voltage is optimized; the simultaneous optimization of voltage and frequency is left for future work.

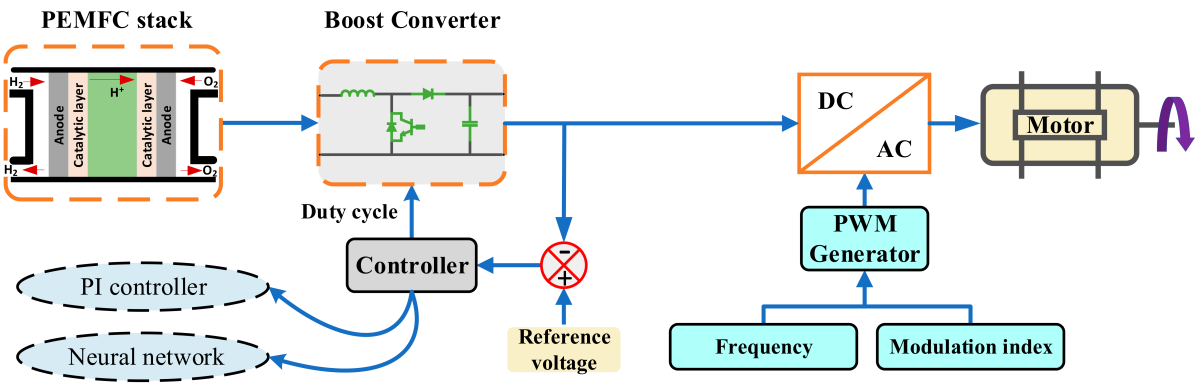


Figure 1. Configuration of the PEMFC-based induction motor drive system.

The remainder of this paper is organized as follows: Section 2 details the system mathematical modeling; Section 3 describes the neural network controller (NNC); Section 4 introduces the DIOA structure; Section 5 presents the simulation and comparative results; and Section 6 provides conclusions and future directions.

2. Mathematical Modelling

This section presents the mathematical modeling of the system components, including the PEMFC, DC–DC converter, and three-phase induction motor.

2.1. PEMFC Stack Model

Mathematically, the PEMFC stack is represented by a detailed semi-empirical model in which the stack voltage is governed by the open-circuit voltage, the activation loss, and the ohmic loss, as shown in Figure 2. Thus, the cell terminal voltage is described by Equation (1) [38].

$$V_{fc} = E_{oc} - N.A.\ln\left(\frac{i_{fc}}{i_0}\right).G_a(s) - i_{fc}.R_{ohm} \quad (1)$$

where V_{fc} is the stack voltage [V], i_{fc} is the stack current [A], N is the number of cells, E_{oc} is the open-circuit voltage [V], i_0 is the exchange current [A], A is the Tafel slope [V], and R_{ohm} is the internal ohmic resistance [Ω]. $G_a(s)$ refers to the charge double-layer effect, which is represented by a first-order lag acting on the activation-voltage term, as given by Equation (2). So, a sudden current change does not instantaneously produce its full activation-voltage drop.

$$G_a(s) = \frac{1}{\left(\frac{s\tau_d}{3} + 1\right)} \quad (2)$$

where τ_d is the response time constant [s].

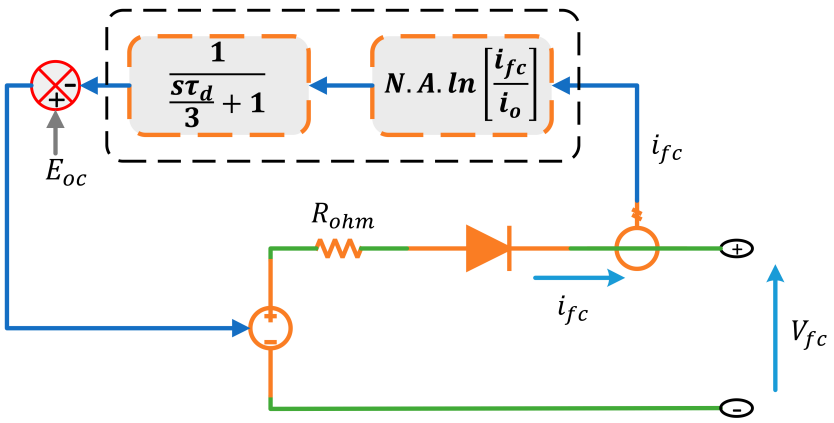


Figure 2. Equivalent electrical model for PEMFC.

The model includes the charge double-layer effect only; gas-supply dynamics (air compressor and manifold filling), pressure oscillations and membrane water transport are not modeled. These slower phenomena would lengthen the transient of the hydrogen flow after a load step, but they do not change the steady-state consumption, which follows Faraday's law through the stack current (Equation (8)) [39].

In fact, E_{oc}, i_0, and A are not fixed. They vary with temperature, pressure, and reactant conditions, as formulated in Equations (3)–(5), respectively [40].

$$E_{oc} = K_c.E_n \quad (3)$$

$$i_0 \propto \left(P_{H_2} + P_{O_2}\right).e^{-\Delta G/RT} \quad (4)$$

$$A = \frac{R.T}{z.\alpha.F} \tag{5}$$

where K_c is a voltage constant and E_n is the Nernst voltage [V]. P_{H_2} and P_{O_2} represent the partial pressures of hydrogen and oxygen, respectively [bar], ΔG and T are the activation energy [J/mol] and stack temperature [K], respectively, z is the number of moving electrons, α is the charge transfer coefficient, R is the universal gas constant [J/mol.K], and F is Faraday's constant [C/mol].

Firstly, the reactant utilizations are determined from the stack current and the supplied fuel/air conditions, as expressed in Equation (6) and Equation (7), respectively [41].

$$U_{fH_2} = \frac{6 \times 10^4.R.T.N.i_{fc}}{z.F.P_{fuel}.V_{fuel}.x\%} \tag{6}$$

$$U_{fO_2} = \frac{6 \times 10^4.R.T.N.i_{fc}}{2z.F.P_{air}.V_{air}.y\%} \tag{7}$$

where P_{fuel} and P_{air} are the absolute supply pressures of fuel and air [bar], respectively. V_{fuel} and V_{air} are the fuel and air flow rates [l/min], and $x\%$ and $y\%$ are the hydrogen and oxygen fractions in the supplied gases, respectively.

Accordingly, the hydrogen consumption rate $V_{H_2,cons}$ [slpm/min] is computed from Equation (8).

$$V_{H_2,cons} = U_{fH_2} V_{fuel} \tag{8}$$

Principally, such utilization factors are then used to compute the gas partial pressures inside the stack as given by Equation (9) and Equation (10), respectively.

$$P_{H_2} = \left[1 - U_{fH_2}\right] . x\% .P_{fuel} \tag{9}$$

$$P_{O_2} = \left[1 - U_{fO_2}\right] . y\% .P_{air} \tag{10}$$

At this moment, the Nernst voltage is updated considering these partial pressures for operating temperature ≤ 100 °C, as revealed in Equation (11) [42].

$$E_n = 1.229 - \frac{(T - 298.15)}{z.F} + \frac{R.T}{z.F} \times \left[ln\left(P_{H_2}\sqrt{P_{O_2}}\right)\right] \tag{11}$$

Finally, the stack power delivered to the DC link P_{fc} [W] is calculated by Equation (12).

$$P_{fc} = V_{fc} \times i_{fc} \tag{12}$$

2.2. Boost DC-DC Converter Model

A boost DC-DC converter increases the input voltage by storing energy in an inductor when the switch is ON and transferring this energy to the output when the switch is OFF. The main components of the converter include an inductor, power switch (MOSFET), diode, output capacitor, and load resistor. For an ideal boost converter operating in continuous conduction mode (CCM), the voltage conversion ratio is given by Equation (13).

$$V_o = \frac{V_{in}}{1 - D} \tag{13}$$

where V_o is the output voltage [V], V_{in} is the input voltage [V], and D is the duty cycle.

In this work, the 537 V DC link equals the peak of the 380 V line voltage of the motor. With the stack voltage of 37–45 V, the required conversion ratio is about 11.9–14.5 (D ≈ 0.9162–0.9311), which is obtained in practice with high step-up topologies such as the interleaved converter in [22]. In the Simulink model, the converter is the boost converter block of the Specialized Power Systems library, set to the average model (D-controlled). This

model is a switching-function model driven directly by the duty-cycle signal D ($0 < D < 1$) delivered by the controller, so that no PWM generator is used and the switching ripple is not represented, the switching losses, the conduction losses of the power switch and the snubber losses are not included. The same converter model is used for the conventional operation (537 V) and for the proposed operation, where the required conversion ratio and duty cycle are lower, so the neglected losses are expected to be smaller in the proposed operation.

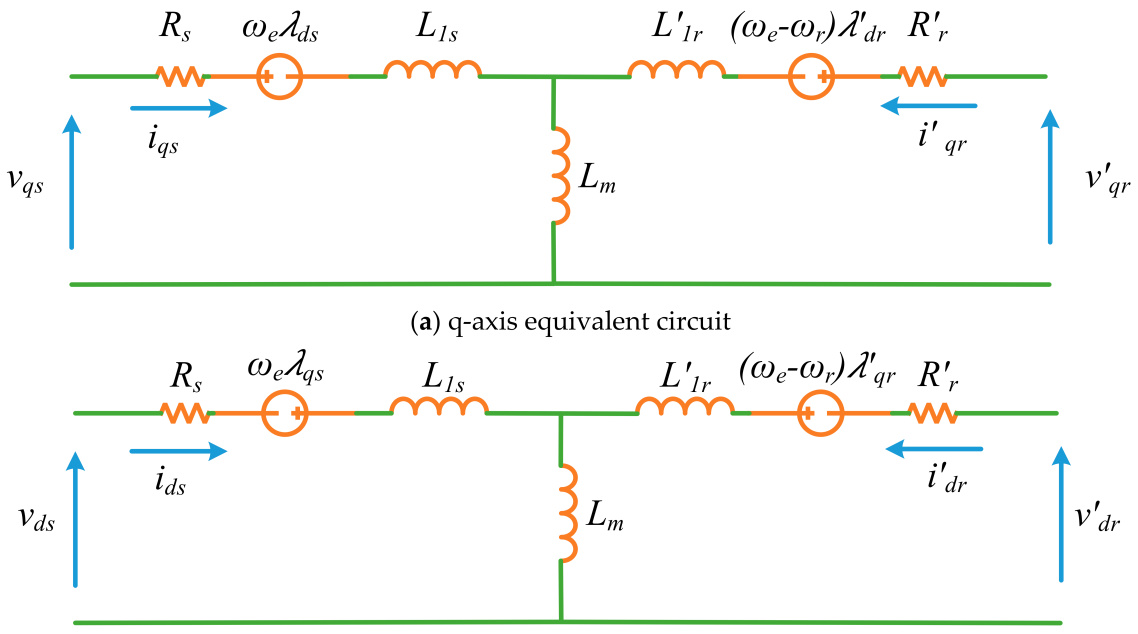
The dynamic equations of the Boost converter can be expressed using state-space averaging in Equations (14) and (15). These expressions clearly indicate the nonlinear relationship between the duty cycle and the output voltage, which motivates the use of intelligent control techniques.

$$\dot{i_L} = \frac{1}{L}\left[V_{in} - (1-D)V_o\right] \tag{14}$$

$$\dot{V_o} = \frac{1}{C}\left[(1-D)i_L - \frac{V_o}{R}\right] \tag{15}$$

2.3. Three-Phase Induction Motor Model

The dynamic behavior of the three-phase induction motor is represented using the well-known synchronously rotating *d-q* reference frame model. Basically, it allows an accurate description of both transient and steady-state operating conditions. In this model, the three-phase stator and rotor variables are transformed into orthogonal *d*- and *q*-axis components. Hence, the corresponding d- and q-axis equivalent circuits of the machine are illustrated in Figure 3a,b, where the electrical relationships between stator and rotor variables are established, respectively [43].



(**a**) q-axis equivalent circuit

(**b**) d-axis equivalent circuit

Figure 3. d-q equivalent circuits of the three-phase induction motor.

Specifically, the stator voltages in the synchronous *d-q* reference frame are expressed as in Equation (16) and Equation (17), respectively [44].

$$\mathcal{V}_{qs} = R_s\, i_{qs} + \frac{d\lambda_{qs}}{dt} + \omega_e\lambda_{ds} \tag{16}$$

$$\mathcal{V}_{ds} = R_s\, i_{ds} + \frac{d\lambda_{ds}}{dt} - \omega_e \lambda_{qs} \tag{17}$$

where $\mathcal{V}_{qs}$ and $\mathcal{V}_{ds}$ represent the stator d- and q-axes voltages [V], respectively. R_s is the stator resistance [Ω], i_{qs} and i_{ds} refer to the stator q- and d-axes currents [A], respectively, λ_{qs} and λ_{ds} are the q- and d-axes flux linkages [Wb], respectively, and ω_e is the synchronous electrical angular velocity of the reference frame [rad/s].

Moreover, the electrical dynamics of the rotor windings, expressed in the synchronous reference frame, are described by Equation (18) and Equation (19), respectively [18].

$$\mathcal{V}'_{qr} = R'_r\, i'_{qr} + \frac{d\lambda'_{qr}}{dt} + (\omega_e - \omega_r)\lambda'_{dr} \tag{18}$$

$$\mathcal{V}'_{dr} = R'_r\, i'_{dr} + \frac{d\lambda'_{dr}}{dt} - (\omega_e - \omega_r)\lambda'_{qr} \tag{19}$$

where $\mathcal{V}'_{qr}$ and $\mathcal{V}'_{dr}$ represent the rotor d- and q-axes voltages [V], respectively. R'_r is the rotor resistance [Ω], i'_{qr} and i'_{dr} refer to the rotor d- and q-axes currents [A], respectively, λ'_{qr} and λ'_{dr} are the d- and q-axes flux linkages [Wb], respectively, and ω_r is the rotor electrical angular velocity [rad/s].

On the other side, the relation that connects the electrical dynamics of the machine with its mechanical motion is given by Equation (20).

$$\omega_r = \omega_m \times p \tag{20}$$

where p is the number of pole pairs and ω_m is the mechanical rotor speed [rad/s].

To complete the electrical model, the flux linkages must be expressed as functions of the stator and rotor currents. In fact, the stator flux is composed of leakage flux and mutual flux produced by both stator and rotor currents. Thus, the stator flux linkages are defined as in Equation (21) and Equation (22), respectively.

$$\lambda_{qs} = L_{1s}\, i_{qs} + L_m\left(i_{qs} + i'_{qr}\right) \tag{21}$$

$$\lambda_{ds} = L_{1s}\, i_{ds} + L_m(i_{ds} + i'_{dr}) \tag{22}$$

where L_{1s} and L_m are the stator leakage inductance and the magnetizing inductance [H], respectively. However, the rotor flux results from both rotor leakage flux and the magnetizing flux linking the stator and rotor windings, as depicted in Equation (23) and Equation (24).

$$\lambda'_{qr} = \left(L'_{1r} + L_m\right) i'_{qr} + L_m i_{qs} \tag{23}$$

$$\lambda'_{dr} = \left(L'_{1r} + L_m\right) i'_{dr} + L_m i_{ds} \tag{24}$$

where L'_{1r} is the rotor leakage inductance [H]. Basically, the torque production is directly determined by the interaction between the stator flux and stator currents, which are controlled by the inverter voltage supplied from the PEMFC-based power system. Hence, the electromagnetic torque developed in the air gap T_e [N.m] can be calculated as in Equation (25) [45].

$$T_e = \frac{3}{2} p\left(\lambda_{ds} i_{qs} - \lambda_{qs} i_{ds}\right) \tag{25}$$

Finally, the mechanical dynamics of the motor shaft are governed by the rotational motion expression as in Equation (26).

$$J\frac{d\omega_m}{dt} = T_e - B.\omega_m - T_L \tag{26}$$

where J is the combined inertia of the rotor and load $\left[\text{kg.m}^2\right]$, T_L is the load torque [N.m], and B is the viscous friction coefficient [N.m.s/rad].

The d–q model of Equations (16)–(26) does not include the iron losses. They are represented in the Simulink model by a core-loss resistance connected in parallel with the three-phase terminals of the motor so that the iron-loss power depends on the applied voltage. The hysteresis and eddy-current losses are lumped in the constant resistance of 1200 Ω; they vary with the square of the terminal voltage. Consequently, reducing the terminal voltage at light load decreases the iron losses together with the stator copper loss, which is the mechanism behind the efficiency improvement reported in Section 5.2. The model assumes a constant core loss resistance, so magnetic saturation and the frequency dependence of the iron losses are not represented, and the branch is connected at the terminals, upstream of the stator resistance.

3. Neural Network Controller

The neural controller that regulates the duty cycle of the boost converter is a NARMA-L2 (feedback-linearization) controller, as shown in Figure 4 and Table 2. It is built in two steps. First, the plant is identified offline. With the regression vector

$$\varphi(k) = \left[y(k), \ldots, y\left(k - n_y + 1\right), D(k-1), \ldots, D(k - n_D + 1)\right] \tag{27a}$$

where y is the output voltage V_o, D is the duty cycle, and $n_y = n_D = 2$ (Table 2), the output voltage of the converter is approximated by

$$\hat{y}(k+1) = f[\varphi(k)] + g[\varphi(k)] \cdot D(k) \tag{27b}$$

where f and g are two feedforward sub-networks, each with one hidden layer of five sigmoid neurons and a linear output neuron. Second, the controller is obtained by solving the identified model for the control input.

$$D(k+1) = \frac{y_{ref}(k+d) - f[\varphi(k)]}{g[\varphi(k)]} \tag{27c}$$

so that the output voltage follows the reference V_{ref} (d is the relative degree). The identification networks are trained offline with the Levenberg–Marquardt algorithm (trainlm) on 150,000 input–output samples. The performance function is

$$J = \frac{1}{2}\sum\nolimits_k [y(k) - \hat{y}(k)]^2 \tag{27d}$$

where V_{ref} is the reference voltage and V_o is the measured output voltage. The backpropagation algorithm is used to update the network weights.

The training data used for the offline identification, i.e., the random plant input (duty cycle) and the corresponding plant output voltage, are shown in Figure 5.

The results shown in Figure 6 confirm the successful identification of the nonlinear plant using a neural network. Also, the network output closely matches the actual plant output while the error signal remains very small, demonstrating accurate system modeling under the excitation input.

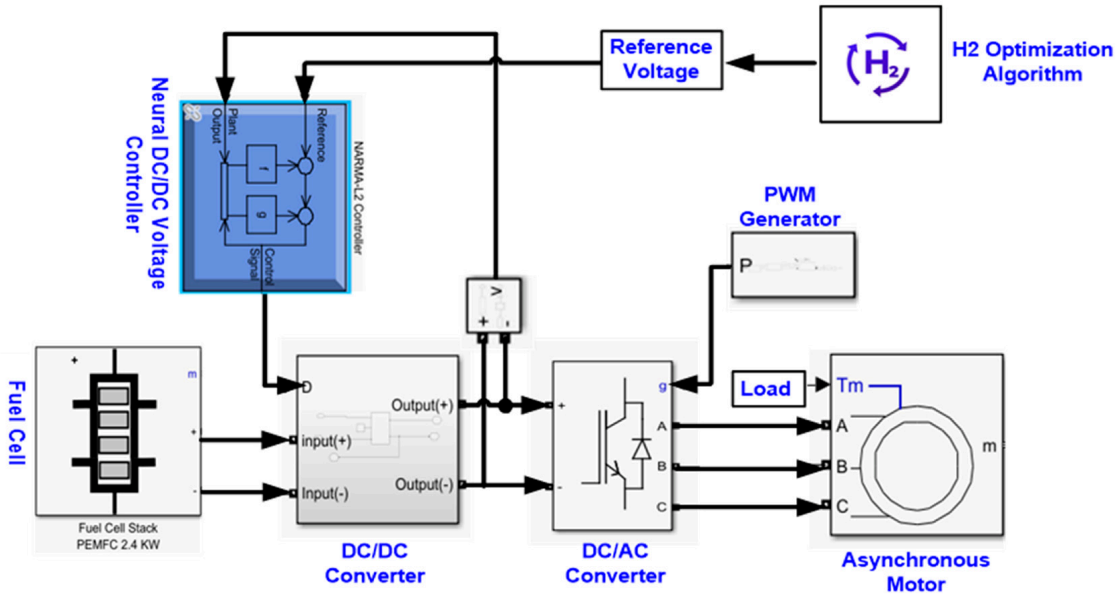


Figure 4. Neural DC to DC voltage controller.

Table 2. Parameters of neural controller.

Section	Parameter	Value
Network Architecture	Size of Hidden Layer	5
	Sampling Interval (sec)	1×10^{-6}
	No. Delayed Plant Inputs	2
	No. Delayed Plant Outputs	2
Training Data	Training Samples	150,000
	Maximum Plant Input	0.92
	Minimum Plant Input	0
	Maximum Plant Output	730
	Minimum Plant Output	−730
	Maximum Interval Value (sec)	0.00012
	Minimum Interval Value (sec)	0.00011
Training Parameters	Training Epochs	100,000
	Training Function	trainlm

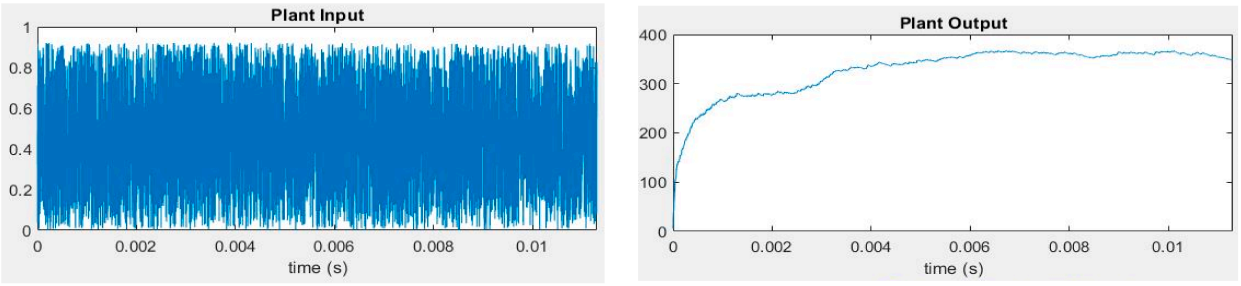


Figure 5. Offline training of neural controller.

The training performance curves in Figure 7 indicate proper convergence of the learning algorithm, where the gradient decreases and the Levenberg–Marquardt parameter is adaptively adjusted.

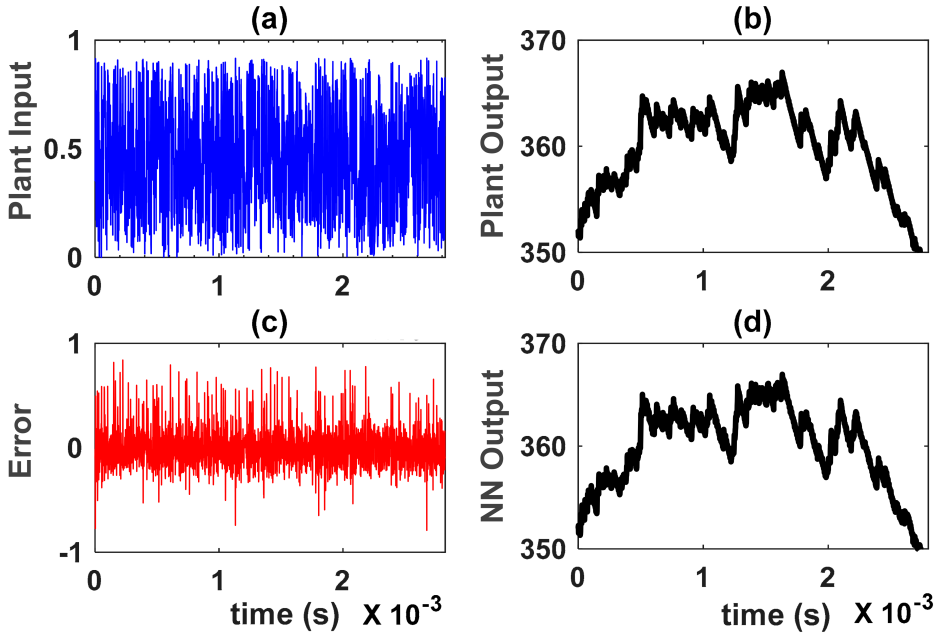


Figure 6. Plant input–output modeling and error analysis: (**a**) plant input, duty cycle (p.u.); (**b**) plant output (V); (**c**) identification error (V); (**d**) NN output (V).

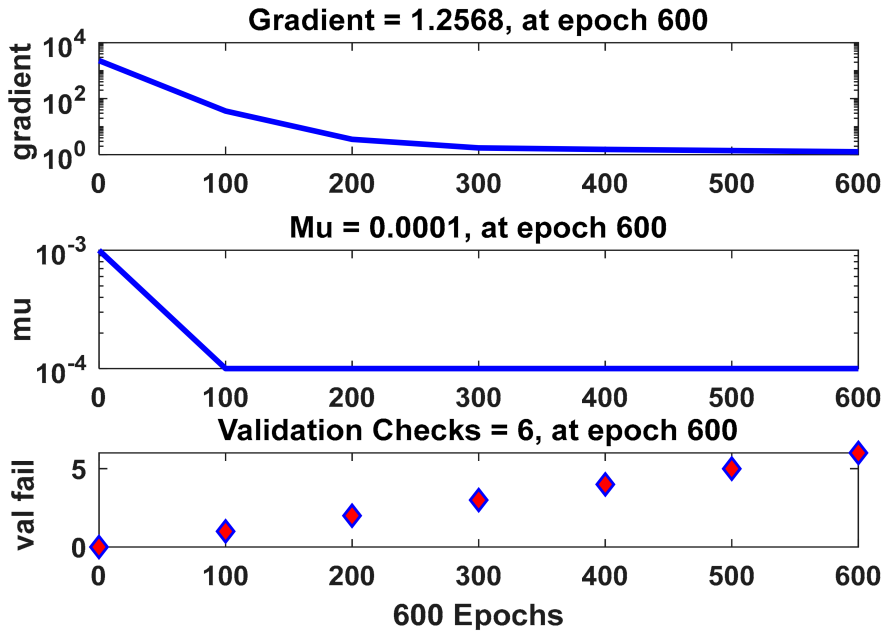


Figure 7. Neural network training convergence parameters.

The training stops based on validation checks, preventing overfitting and ensuring good generalization. The regression analysis in Figure 8 shows correlation coefficients close to unity ($R \approx 0.999$), indicating an almost perfect agreement between predicted and actual outputs across training, validation, testing, and overall datasets.

Furthermore, the performance plot in Figure 9 illustrates a minimum mean squared error of approximately 0.03 at the optimal epoch, confirming the high accuracy of the model. Overall, the neural network effectively captures the plant dynamics with excellent precision and strong generalization capability, making it suitable for nonlinear system modeling and control applications.

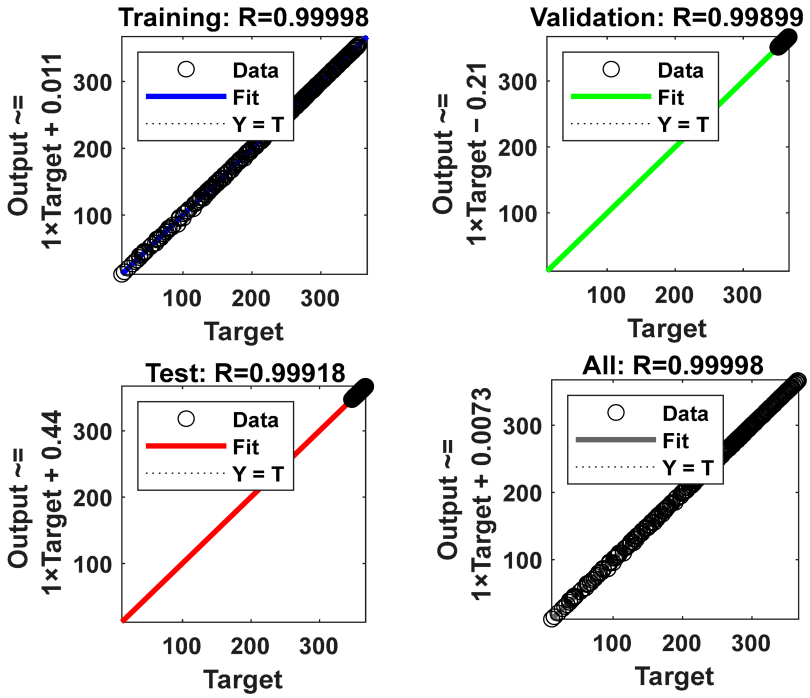


Figure 8. Regression analysis of neural network performance.

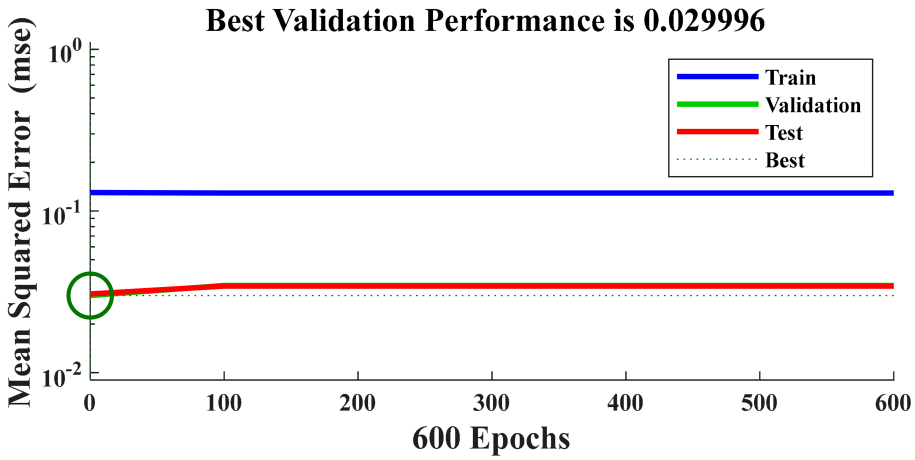


Figure 9. Best validation performance (MSE curve). The validation curve (green) almost coincides with the test curve (red) and is therefore hidden behind it; the green circle and the green dotted line indicate the best validation performance.

4. Dholes-Inspired Optimization Algorithm

The dholes-inspired optimization algorithm (DIOA) is a contemporary swarm-based metaheuristic optimization strategy, developed by Romeh A.E. et al. in 2025 [46]. It replicates the collaborative hunting behavior of dholes. The dhole is a very gregarious species of the Canidae family, native to the grasslands and forests of Southeast, Central, and East Asia, and is popularly referred to as the Asian wild dog. Dholes are famous for their cooperative hunting activities, complicated social structures, and advanced vocal systems of communication. In contrast to current swarm-based techniques like PSO and grey wolf optimization, the DIOA uses a multiple-stage leadership paradigm in which a dynamically chosen lead vocalizer directs the process of search. Furthermore, the DIOA uses a vocalization-based guiding mechanism, in which the effect of the lead vocalizer progressively diminishes over iterations, distinguishing it from the completely random exploration observed in other

bio-inspired techniques. Based on the sophisticated social behaviors of dholes, the DIOA simulates their cooperative hunting techniques, vocal communication, and territorial instincts for implementing a robust metaheuristic approach to solve challenging optimization problems. Figure 10 demonstrates the flowchart of the DIOA, describing the operation sequence from initialization to convergence [46].

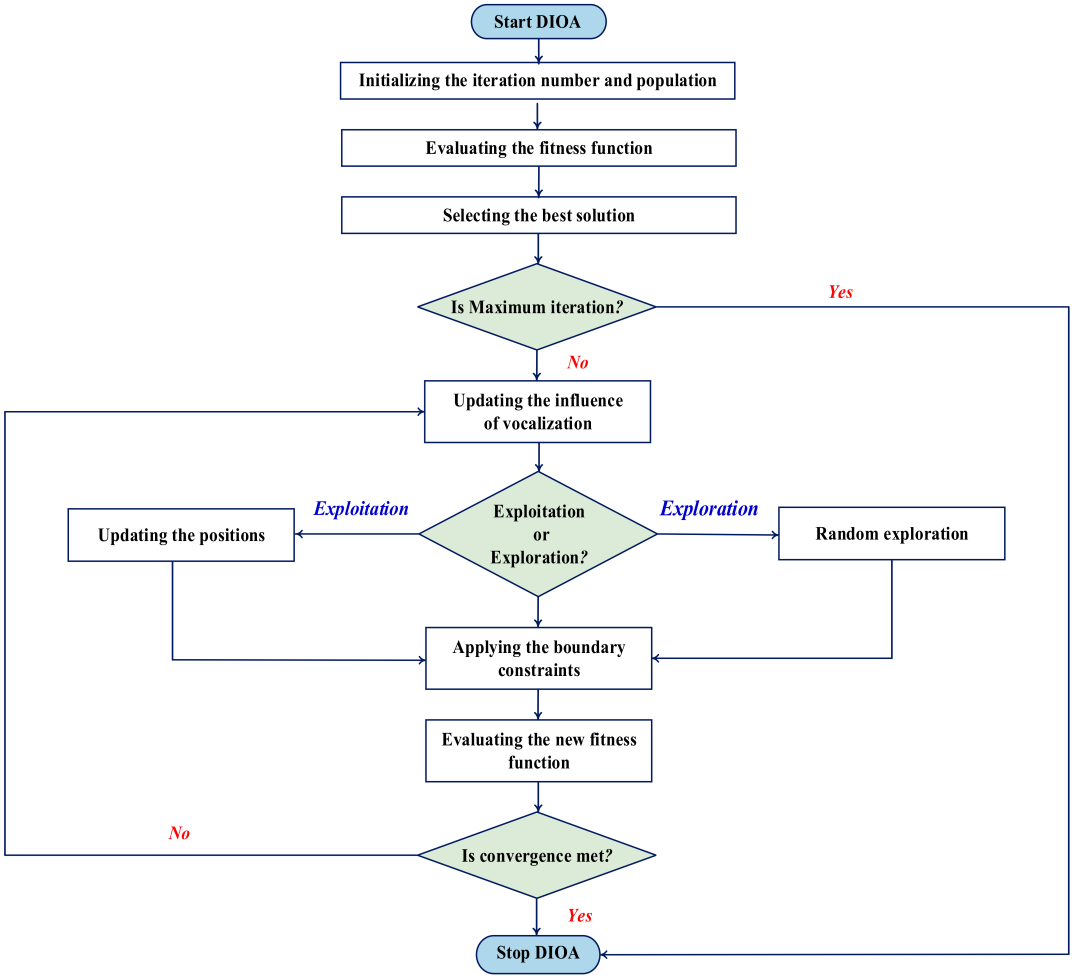


Figure 10. The flowchart of the DIOA.

The first step in implementing the DIOA is to randomly initialize a set of candidate solutions, each of which represents a dhole in the area of search. Then, the position of each candidate solution is iteratively refined based on the influence of vocalization, cooperative hunting modifications, and territorial constraints. In each iteration, the lead vocalizer, which directs the process of optimization, is the most optimum candidate solution. Every possible solution readjusts its proximity to the optimal solution. The impact of vocalization guarantees a balance between exploitation and exploration. The impact of the lead vocalizer progressively wanes over iterations, enabling a regulated shift from wide exploration to intensive exploitation. The diminution of this impact is mathematically expressed by Equation (28):

$$V_{oc} = 2 - it\left(\frac{2}{it_{max}}\right) \tag{28}$$

where V_{oc} represents the impact of vocalization, it indicates the current iteration number, and it_{max} refers to the maximum number of iterations. This formula guarantees that the early iterations promote varied exploration throughout the space of search. In subsequent iterations, the search is refined by concentrating on promising solutions. The gradual

decrease in V_{oc} imitates how dholes switch their dependance from vocal communication to direct coordination when they get close to their target [46].

Dholes have very coordinated hunting techniques, where the members of pack dynamically modify their movements according to nearby individuals and the lead vocalizer. The position update technique of the DIOA incorporates this cooperative behavior, as demonstrated in Figure 10. The trade-off between exploration and exploitation determines whether a search agent explores new areas of the solution space or focuses on improving promising solutions that have been found previously. A scaling factor β is included to regulate the intensity of movement exhibited by the search agents. Equation (29) provides a mathematical definition of this factor, which is directly impacted by the vocalization effect:

$$\beta = V_{oc}\, m \tag{29}$$

where m is a randomly selected number drawn from a uniform distribution within the interval from zero to one. This formula guarantees that the intensity of movement is dynamically modified, enabling extensive exploration in the first phases of the search while progressively enhancing movements as convergence becomes approach. A sinusoidal function is used to calculate a coefficient C_o, which is used to incorporate regulated oscillations into the dynamics of movement. The mathematical expression of coefficient C_o is shown in Equation (30):

$$C_o = m + \sin(\pi\, m) \tag{30}$$

The sinusoidal part in Equation (30) provides regulated fluctuations in movement, avoiding early convergence by guaranteeing the search remains flexible and does not become too rigid. This characteristic permits the agents of search to preserve a degree of randomness, hence boosting the possibility of escaping local optimal solutions [46].

After the coefficients of movement control have been calculated, the following step includes finding the controlled Euclidean distance ($\vec{d_{lead}}$) between the lead vocalizer and each search agent. The computation of distance includes the coefficient C_o for adaptive modifications, as indicated in Equation (31):

$$\vec{d_{lead}} = \left| C_O\, \vec{P_{LV}}^{\,2} - \vec{d_i}^{\,2} \right| \tag{31}$$

where $\vec{P_{LV}}$ is the lead vocalizer position and $\vec{d_i}$ indicates the current position of the search agent indexed by i. The coefficient C_o dampens or amplifies the adjustments of movement, guaranteeing that the search stays aggressive in the first iterations and becomes more precise as it advances. After the controlled distance to the lead vocalizer is calculated, the new position for the agent of search is updated according to Equation (32).

$$\vec{x_{lead}} = \vec{P_{LV}} + s\, \sqrt{\vec{d_{lead}}} \tag{32}$$

Equation (32) guarantees that every search agent advances toward the lead vocalizer weighted by the square root of $\vec{d_{lead}}$ and an intensity scale (s). Therefore, this leads to preventing irregular jumps and smoothing the movement dynamics. The cooperative hunting approach, as formulated in equations from Equation (29) to Equation (32), enables search agents to dynamically follow the lead vocalizer while keeping a well-regulated balance between exploitation and exploration [46].

The DIOA uses the boundary constraints for preventing the agents of search from deviating beyond the range of possible solutions. Equation (33) provides a mathematical definition of this mechanism in order to avoid the excessive divergence.

$$\vec{d_i} = \begin{cases} LB + (UB - LB) * \ rand(\dim) & if\ \vec{d_i} < LB\ or\ \vec{d_i} > UB \\ \vec{d_i} & otherwise \end{cases} \tag{33}$$

where UB and LB define the upper and lower bounds for the space of search, respectively. The rand function provides a random number guaranteeing that any solution breaching

the constraints is re-placed inside valid boundaries. The agent of search with the optimum value of fitness function is set as the lead vocalizer at each iteration end, guaranteeing that the DIOA continuously tracks the most optimal possible solution path. Equation (34) provides a mathematical definition of this mechanism in order to select the lead vocalizer.

$$\overrightarrow{Lead_{Vocalizer}} = \begin{cases} \overrightarrow{d_i} & if\ fitness\ (\overrightarrow{d_i}) < fitness\ (\overrightarrow{Lead_{Vocalizer}}) \\ \overrightarrow{Lead_{Vocalizer}} & otherwise \end{cases} \quad (34)$$

The quality of each potential solution is assessed by the fitness function, which replaces the current lead vocalizer in the subsequent iteration if it is discovered that a search agent is more suited than the current lead vocalizer. The DIOA stops when the maximum iteration number is reached or when the improvement in fitness is smaller than a predetermined threshold. These restrictions limit unnecessary computational effort while guaranteeing the algorithm to reliably converge to the optimum solution [46].

5. Simulation Results

5.1. System Description and Baseline Performance

The modeling of proposed system is carried out by the Simulink/Matlab software tool. Table 3 shows the parameters of the three-phase induction motor and Table 4 illustrates the parameters of the PEMFC stack, where the motor parameters are those of the actual (physical) induction motor and the PEMFC stack parameters are the preset values of the PEMFC stack block of the MATLAB/Simulink library. Figure 11 shows the variations in the PEMFC stack voltage and power with the load.

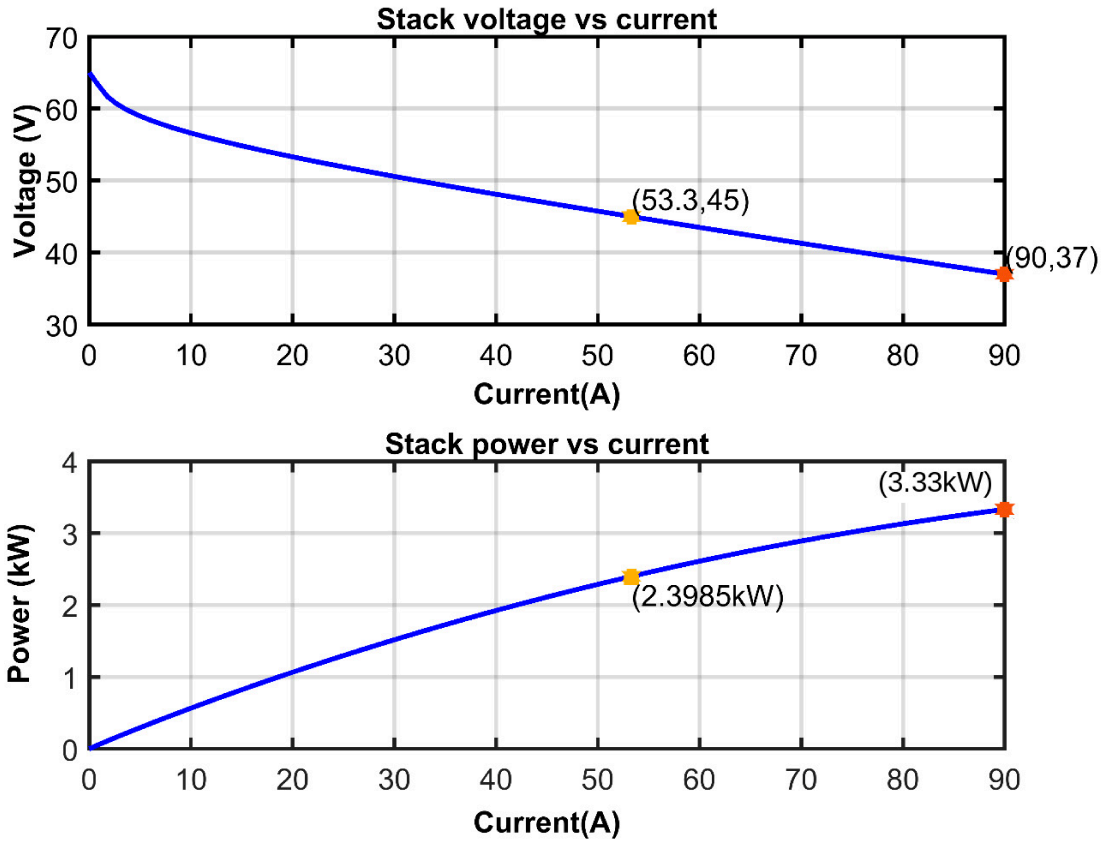


Figure 11. Variations in PEMFC stack voltage and power with load current.

Table 3. The parameters of the three-phase induction motor.

Rated output	2 hp
Rated voltage	220/380 V
Number of poles	4
Supply frequency	50
Stator winding resistance	5.60 Ω
Leakage winding inductance	16.65 mH
Referred rotor winding resistance	4.40 Ω
Referred leakage winding inductance	16.65 mH
Magnetizing inductance	245.20 mH
Core loss resistance	1200 Ω

Table 4. The parameters of the PEMFC stack.

Stack nominal power	2398.5 W
Stack maximum power	3330 W
Fuel cell resistance	0.18881 Ω
Nernst cell voltage	1.1288 V
Number of cells	65
Nominal current and voltage	53.3 A/45 V
Maximum current/voltage	90 A/37 V
Open-circuit voltage	65 V
Nominal H2 utilization	99.56%
Nominal O2 utilization	59.28%
Nominal fuel consumption	24.14 slpm
Nominal air consumption	57.46 slpm
Exchange current (i_0)	0.41218 A
Exchange coefficient (α)	0.46322
Fuel composition (H_2)	99.95%
Oxidant composition (O_2)	21%
Nominal fuel rate at nominal H_2 utilization	20.02 lpm
Maximum fuel rate at nominal H_2 utilization	33.8 lpm
Nominal air rate at nominal O_2 utilization	120 lpm
Maximum air rate at nominal O_2 utilization	202.6 lpm
System temperature	338 Kelvin
Fuel supply pressure	1.5 bar
Air supply pressure	1 bar

5.2. Optimization of Reference Voltage for Hydrogen Minimization

PSO and the DIOA are employed to obtain the optimal reference voltage for the controller of the DC boost converter for minimizing hydrogen consumption by the fuel cell while maintaining motor load performance. The optimal reference voltages for the controller of the boost converter are obtained at every load torque from 0.5 to 10 N.m with a step of 0.5. The two optimization techniques are operated for three trials at every load torque, and the best solution with the lowest objective function is taken. The population size and iteration number are 10 and 10, respectively, for the two optimization methods.

Unlike classical loss-model controllers [33–37], which give the optimal flux from the motor parameters under a sinusoidal supply, the present optimization minimizes the hydrogen consumption of the complete system. It therefore also accounts for the converter and inverter losses, the harmonic losses of the PWM supply and the nonlinear polarization curve of the stack. Since the motor losses are dominant, the obtained voltages are expected to be close to the loss-model optimum, with small differences due to these additional effects.

All simulations were run in MATLAB/Simulink [MATLAB 2019b] on a computer with an Intel Core i7-9750H processor and 16 GB RAM using a fixed-step discrete solver with

a sample time of 5×10^{-5} s. One optimization run (population size 10 and 10 iterations) requires 100 simulation evaluations, each taking about 1–4 min. The hydrogen consumption QH2 is the mean value over the steady-state window t = 4–5 s. The optimization is performed offline, and the resulting optimal voltage-load torque map is stored as a lookup table; hence, the computation time does not affect the online operation of the drive.

Figure 12 shows the schematic diagram of the proposed system in the Simulink. The objective function (Obj_1) is achieved by the variation in one input variable; the magnitude of reference voltages for the controller of the boost converter (V_{ref}) at every load torque to minimize consumed hydrogen by fuel cell are illustrated in Equation (35).

$$Obj_1 = minimize\ (Q_{H_2,cons}) \text{ with constraints } (T_e = T_L) \tag{35}$$

where $Q_{H_2,\text{cons}}$ is the consumed hydrogen by fuel cell.

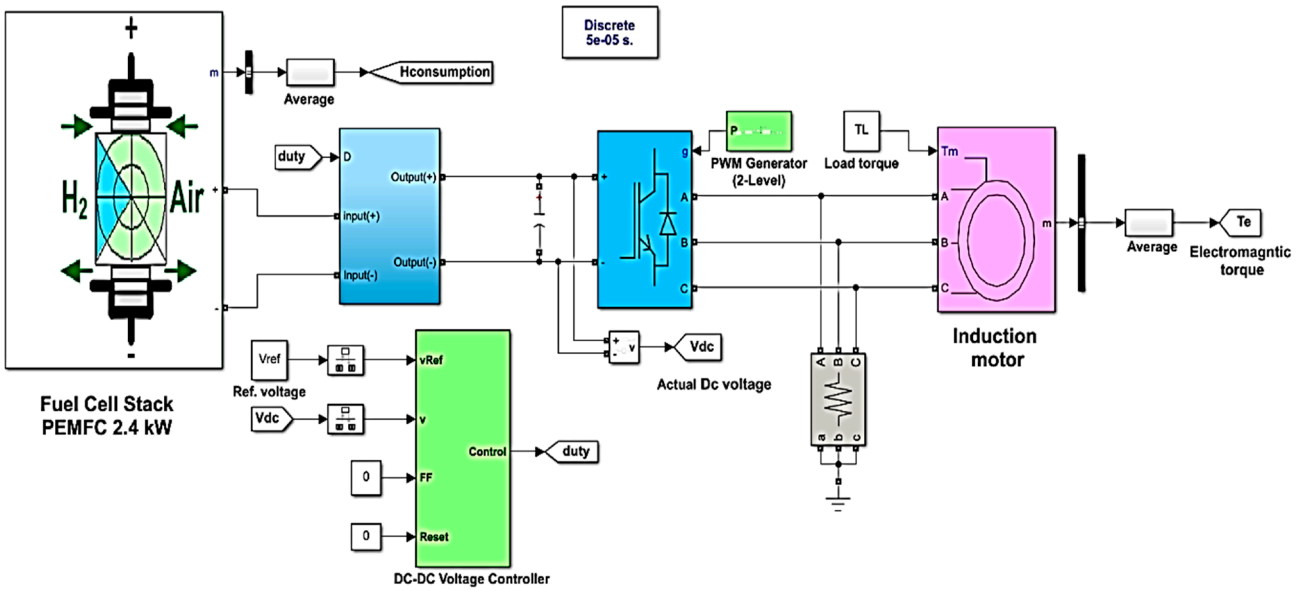


Figure 12. A schematic diagram of proposed system in the Simulink.

Table 5 depicts the comparison between the DIOA and PSO for load torques from 0.5 to 10 N.m with a step of 0.5. The comparison between the two optimization approaches is in terms of the values of the objective function and the optimal reference voltages for the boost converter controller.

Figure 13 shows the convergence curves of the optimization algorithm objective function (Obj_1) with iterations based on PSO and the DIOA at load torques equal to 0.5 and 7.5 N.m.

The percentage saving in hydrogen consumption with the proposed method can be calculated using Equation (36).

$$H_2\ Saving = \frac{Conventional\ Q_{H_2,\text{cons}} - Proposed\ Q_{H_2,\text{cons}}}{Conventional\ Q_{H_2,\text{cons}}} \times 100 \tag{36}$$

Table 6 compares the classical operation, with the converter output voltage fixed at 537 V, and the proposed operation with the optimal DC-link voltage obtained by the DIOA. At 0.5 N·m, the optimal voltage of 132.76 V reduces the hydrogen consumption from 1.9991 to 0.7067 slpm (64.65%). The saving drops to 24.17% at 2 N·m and becomes negligible above 8.5 N·m, where the optimal voltage approaches 537 V. At the same load torque, the reduced voltage increases the slip and lowers the speed, so the output power of the proposed operation is lower by up to about 7% (e.g., 1396.1 rpm and 73.06 W instead of

1494.6 rpm and 78.22 W at 0.5 N·m). This is expected, since Equation (35) minimizes the hydrogen consumption at a given torque without constraining the speed. Minimizing the hydrogen consumption per unit of output power is left for future work.

Table 5. Comparison between two optimization techniques for hydrogen consumption minimization (Obj_1).

T_L N m	PSO		DIOA	
	Obj_1 (slpm)	V_{ref} (V)	Obj_1 (slpm)	V_{ref} (V)
0.5	0.706698	132.698682	0.706726	132.756543
1.0	1.455105	179.230214	1.455219	178.287207
1.5	2.227313	222.706616	2.227312	222.662953
2.0	3.019569	258.537802	3.019592	258.782062
2.5	3.830193	289.062871	3.830121	288.128901
3.0	4.663921	328.797507	4.663379	328.039701
3.5	5.505192	335.940577	5.505773	333.980797
4.0	6.377953	346.582666	6.378596	346.029006
4.5	7.255051	374.519398	7.255702	373.646156
5.0	8.153650	400.465286	8.153538	400.779498
5.5	9.072650	425.954308	9.072650	426.002154
6.0	10.013909	443.755817	10.014316	448.694827
6.5	10.976487	463.243195	10.976492	462.687867
7.0	11.964231	486.955786	11.965154	488.870253
7.5	12.972080	498.502832	12.972082	498.533334
8.0	14.006600	514.890746	14.006593	514.809209
8.5	15.068156	530.725836	15.068163	530.813797
9.0	16.161088	537.000000	16.161092	536.993469
9.5	17.302353	537.000000	17.302403	536.974697
10.0	18.499552	537.000000	18.499556	536.998875

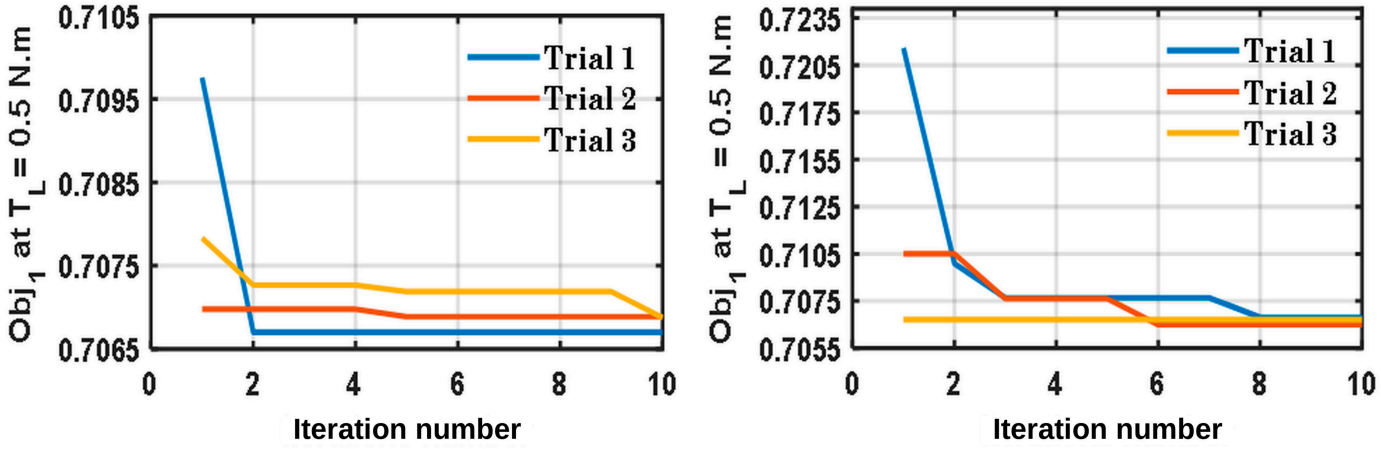
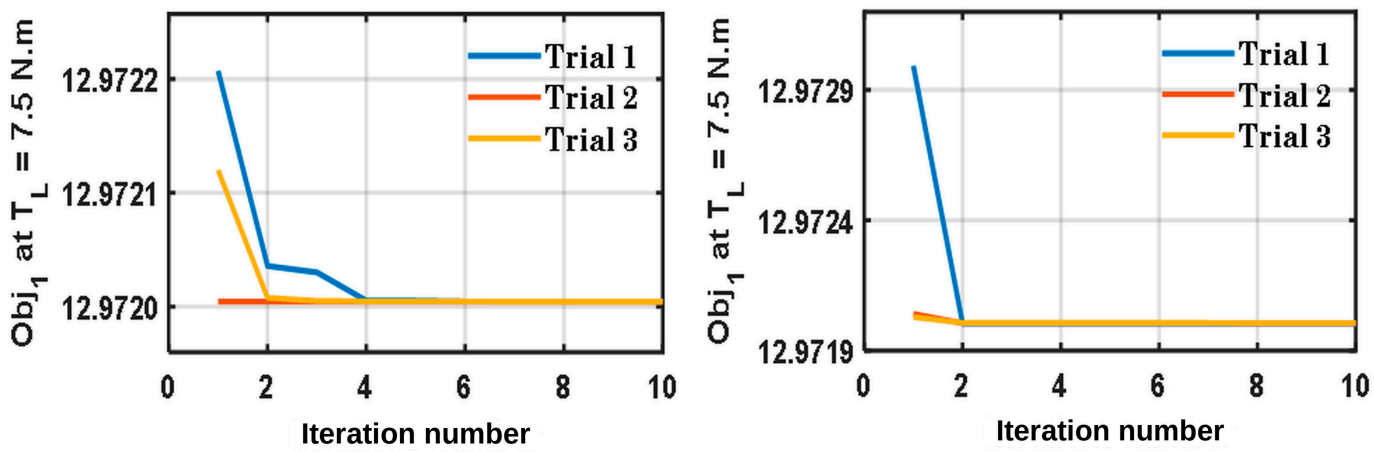


Figure 13. *Cont.*



(**a**) PSO (**b**) DIOA

Figure 13. The convergence curve of Obj_1 with iterations for three trials at certain load torques: (**a**) PSO; (**b**) DIOA.

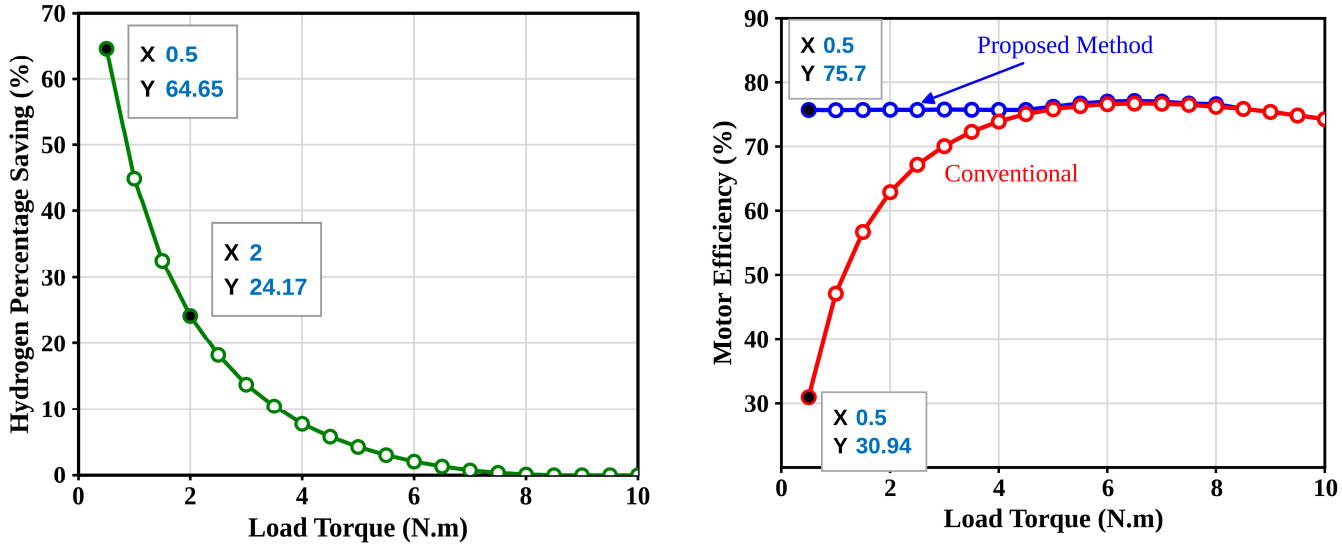
Table 6. Hydrogen consumption and motor performance under classical (537 V) and DIOA-optimized operation.

T_L (N.m)	Classical Operation DC-Link Voltage = 537 V			DIOA			
	$Q_{H2,cons}$ (slpm)	Speed (rpm)	P_{out} (*Watt*)	V_{ref} (V)	$Q_{H2,cons}$ (slpm)	Speed (rpm)	P_{out} (*Watt*)
0.5	1.999121	1494.622807	78.2186	132.756543	0.706726	1396.1067	73.0629
1.0	2.640421	1489.138276	155.8631	178.287207	1.455219	1381.8040	144.6288
1.5	3.301407	1483.558478	232.9187	222.662953	2.227312	1387.5030	217.8380
2.0	3.982114	1477.877642	309.3691	258.782062	3.019592	1389.3286	290.8328
2.5	4.682756	1472.089587	385.1968	288.128901	3.830121	1388.1860	363.2420
3.0	5.404138	1466.187534	460.3829	328.039701	4.663379	1398.3792	439.0911
3.5	6.147003	1460.164202	534.9068	333.980797	5.505773	1382.2515	506.3648
4.0	6.912318	1454.011655	608.7462	346.029006	6.378596	1372.3610	574.5618
4.5	7.701228	1447.721237	681.8767	373.646156	7.255702	1378.15790	649.1124
5.0	8.515055	1441.283477	754.2717	400.779498	8.153538	1383.4765	724.0194
5.5	9.355314	1434.687982	825.9020	426.002154	9.072650	1378.2189	793.3947
6.0	10.223735	1427.923302	896.7358	448.694827	10.014316	1389.5627	872.6454
6.5	11.122291	1420.976780	966.7379	462.687867	10.976492	1386.9585	943.5941
7.0	12.053242	1413.834361	1035.8693	488.870253	11.965154	1392.1102	1019.9527
7.5	13.019179	1406.480380	1104.0871	498.533334	12.972082	1388.0203	1089.5959
8.0	14.023087	1398.897294	1171.3433	514.809209	14.006593	1387.9927	1162.2126
8.5	15.068430	1391.065346	1237.5845	530.813797	15.068163	1388.0906	1234.9379
9.0	16.159253	1382.962177	1302.7504	536.993469	16.161092	1383.1833	1302.9587
9.5	17.300319	1374.562329	1366.7731	536.974697	17.302403	1374.7695	1366.9791
10.0	18.497289	1365.836627	1429.5757	536.998875	18.499556	1366.0561	1429.8054

Figure 14 shows that the hydrogen saving results mainly from the improvement in motor efficiency. At rated flux and light load, the core and copper losses are large compared with the output power, and the efficiency is only 30.94% at 0.5 N·m. Reducing the voltage according to the load lowers these losses and keeps the efficiency at about 75.7% up to 4.5 N·m. At higher loads the two curves converge and coincide above 8.5 N·m.

From the results based on hydrogen consumption minimization (Obj_1), the hydrogen consumption by the fuel cell increases with increasing the load torque for both techniques. Both PSO and the DIOA achieve nearly identical objective function values (Obj_1) across

all load torques, with deviations typically less than 0.01%. To verify that these solutions are optimal, a direct voltage sweep was performed at 2 and 6.5 N·m. It showed a single minimum at each load, in agreement with the DIOA results.



(**a**) Hydrogen percentage saving with proposed method (**b**) Motor efficiency with classical and proposed methods

Figure 14. System performance under varying load torques: (**a**) hydrogen percentage saving and (**b**) motor efficiency comparison.

Both algorithms use the same population size and number of iterations, i.e., the same number of objective-function evaluations (100 per run), so their computational cost is the same and is dominated by the Simulink simulation of each evaluation. In terms of solution quality, the DIOA and PSO give nearly identical objective values, and the reference voltages agree within about 1.1%. The largest voltage difference (6.0 N·m) changes the hydrogen consumption by only 0.004%, because the objective function is flat near its minimum.

After the optimal values of reference voltages for the boost converter controller are obtained based on Obj_1 for load torques from 0.5 to 10 N.m, these optimal values are used as a reference value for the boost converter controller to track the output voltage of the boost converter for minimizing the hydrogen consumption.

The optimal voltage is a function of the load torque, which is not measured in practice. In steady state the electromagnetic torque (T_e) equals the load torque (T_L) and T_e can be estimated from the measured stator voltages and currents; the estimated torque then addresses the optimal voltage lookup table. The influence of the estimation error on the hydrogen saving is not investigated in this paper.

5.3. Optimal PI Controller Tuning and Dynamic Response

The gains of the PI controller significantly influence the dynamic performance and voltage regulation capability of the boost converter. Therefore, both the DIOA and PSO are used to determine the optimal values of the PI controller gains (K_p and K_i). The optimization process aims to minimize the Integral Time Absolute Error for the difference between the actual output voltage of the DC–DC boost converter and its reference voltage, denoted as ($ITAE_{Vdc}$). The objective function, (Obj_2), is formulated as given in Equation (37).

$$Obj_2 = minimize\ (ITAE_{Vdc}) \tag{37}$$

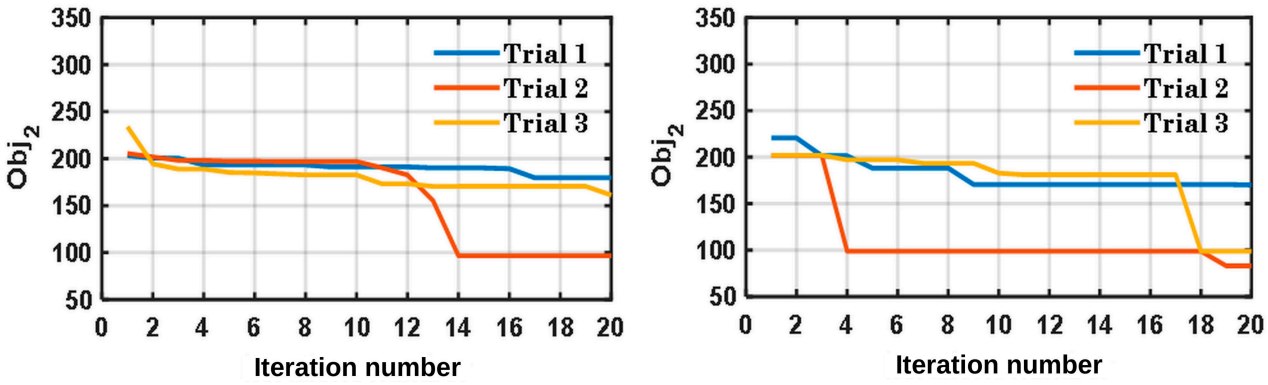
The two optimization techniques are operated for three trials at every load torque, and the best solution with the lowest objective function is taken. The population size and

iteration number are 20 and 20, respectively, for the two optimization methods. Table 7 depicts the comparison between the DIOA and PSO for (Obj_2). The comparison between the two optimization approaches is in terms of the values of the objective function and the optimal PI gains of the boost converter.

Table 7. Comparison between two optimization techniques for integral absolute error minimization (Obj_2).

	Obj_2	K_p	K_i
PSO	96.6540974572087	0.000604570779424463	0.0247152924603185
DIOA	83.1219692544369	0.000696036533653436	0.0287569356768777

Figure 15 shows the convergence curves of the objective function (Obj_2) for the DIOA and PSO over the trials performed. The dynamic responses of the boost converter output voltage with the two tuned PI controllers are presented in Figure 16. The best ITAE values obtained are 83.12 with the DIOA and 96.65 with PSO. Because only three trials were performed and the final values vary from trial to trial, this difference is not considered sufficient to rank the two algorithms. Both tuned controllers track the reference voltage with similar accuracy and speed.



(**a**) PSO (**b**) DIOA

Figure 15. The convergence curve of Obj_2 with iterations for three trials: (**a**) PSO; (**b**) DIOA.

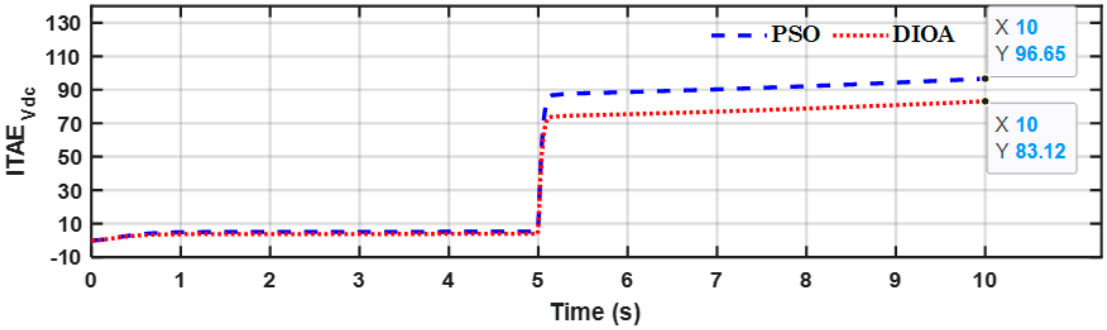
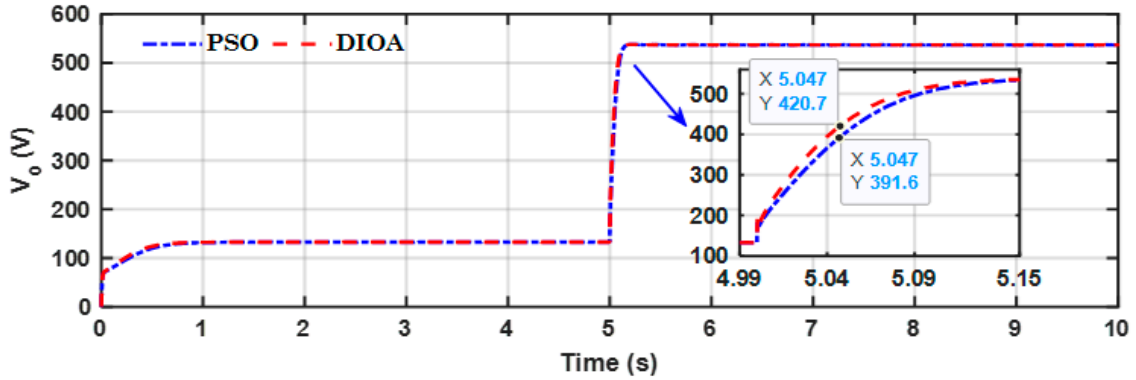
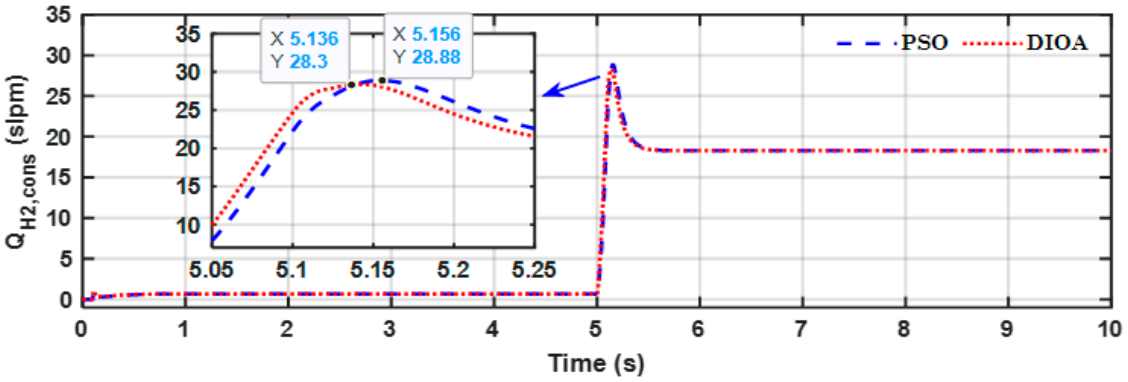


Figure 16. ITAE simulation results using the optimal PI controller gains obtained by DIOA and PSO.

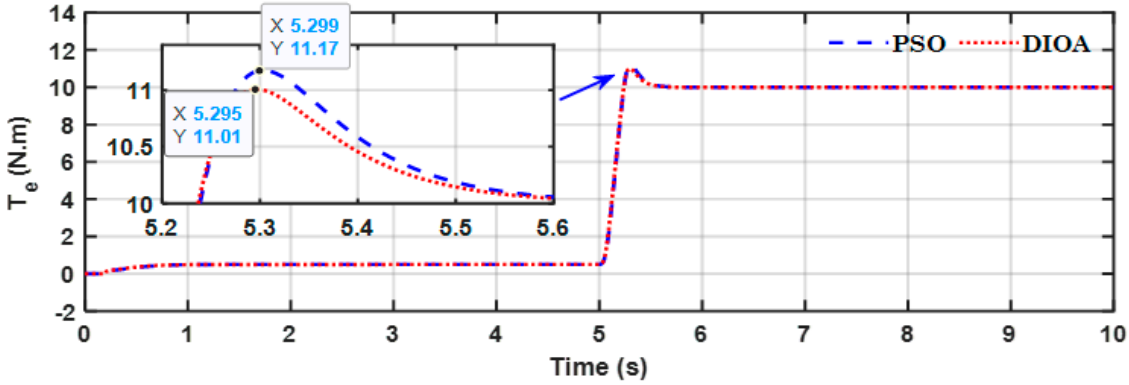
The robustness and dynamic performance of the proposed system with the optimally tuned PI controller were assessed by applying a step increase in load torque from 0.5 N·m to the rated load torque of 10 N·m at a time of 5 s. The corresponding responses of hydrogen consumption, motor torque, and motor speed are illustrated in Figure 17a–d.



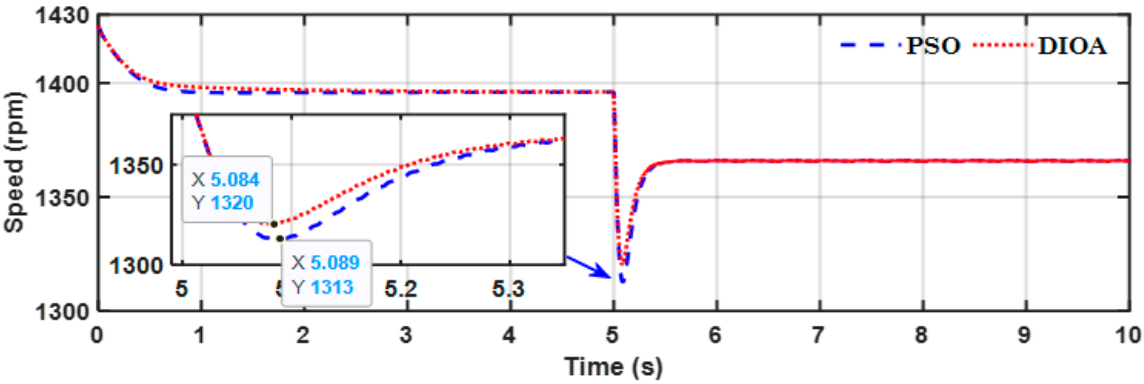
(**a**) DC-DC converter output voltage



(**b**) Hydrogen consumption (slpm)



(**c**) Motor electromagnetic torque



(**d**) Motor speed

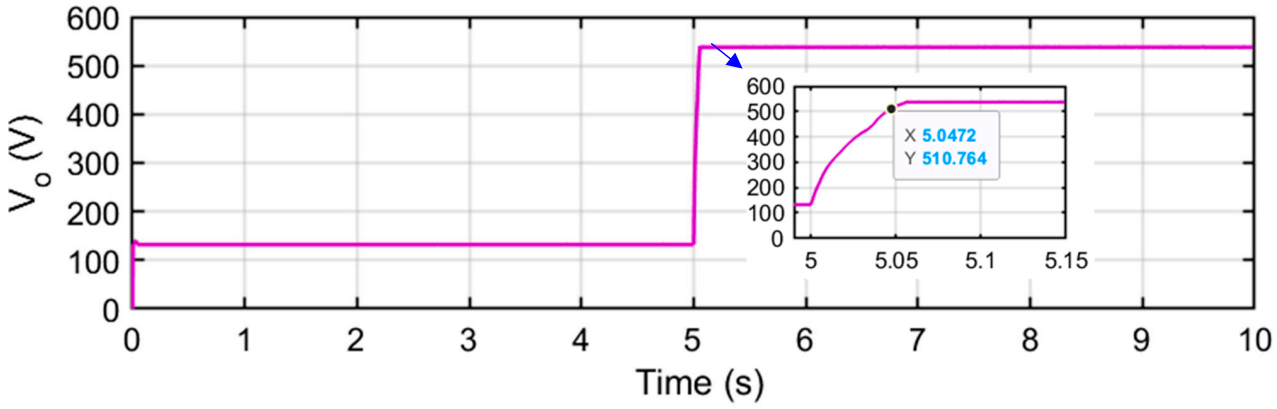
Figure 17. Simulation results obtained using the optimal PI gains of the boost converter controller: (**a**) DC–DC converter output voltage, (**b**) fuel cell hydrogen consumption, (**c**) induction motor electromagnetic torque, and (**d**) induction motor speed.

The results show that the system effectively accommodates the sudden load disturbance and restores steady-state operation within approximately 0.6 s. Following the load increase, the DC–DC converter output voltage continues to track the reference voltage effectively, while the hydrogen consumption rises from 0.706726 slpm to 18.499556 slpm. The transient peak reaches about 28.88 slpm with PSO tuning and 28.3 slpm with DIOA tuning. Simultaneously, the motor torque increases from 0.5 N·m to 10 N·m to satisfy the load demand, with a maximum transient value of approximately 11 N·m.

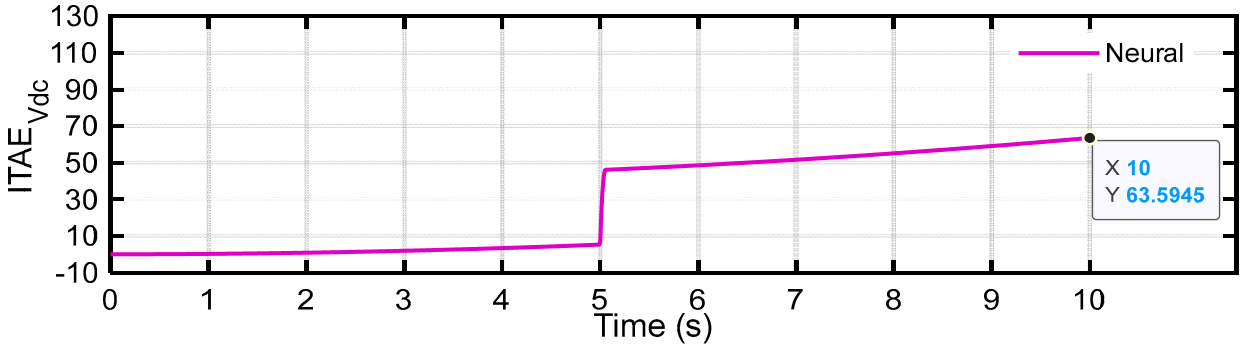
The motor speed decreases from approximately 1395 rpm to a new steady-state value of 1366 rpm after the load change (the synchronous speed is 1500 rpm) restores steady-state operation within approximately 0.6 s; this time refers to the electrical response of the converter–motor system, since the gas-supply dynamics are not modeled (Section 2.1). The minimum speed attained during the transient period is approximately 1313 rpm for the PSO-based controller and 1320 rpm for the DIOA-based controller. These results confirm the ability of both optimization methods to maintain stable operation under severe load variations, and the two tuned controllers give comparable transient performance.

5.4. Performance Evaluation of the Neural Network Controller (NNC)

The dynamic response of the system employing the NNC was evaluated under the same step change in load torque from 0.5 N·m to 10 N·m applied at a time of 5 s. The corresponding results are presented in Figures 18 and 19. As shown in Figure 18a,b, the NNC provides a faster voltage response to the load disturbance compared with the optimally tuned PI controller. This improvement is reflected by a lower ITAE value of 63.59, indicating enhanced tracking performance and transient behavior.

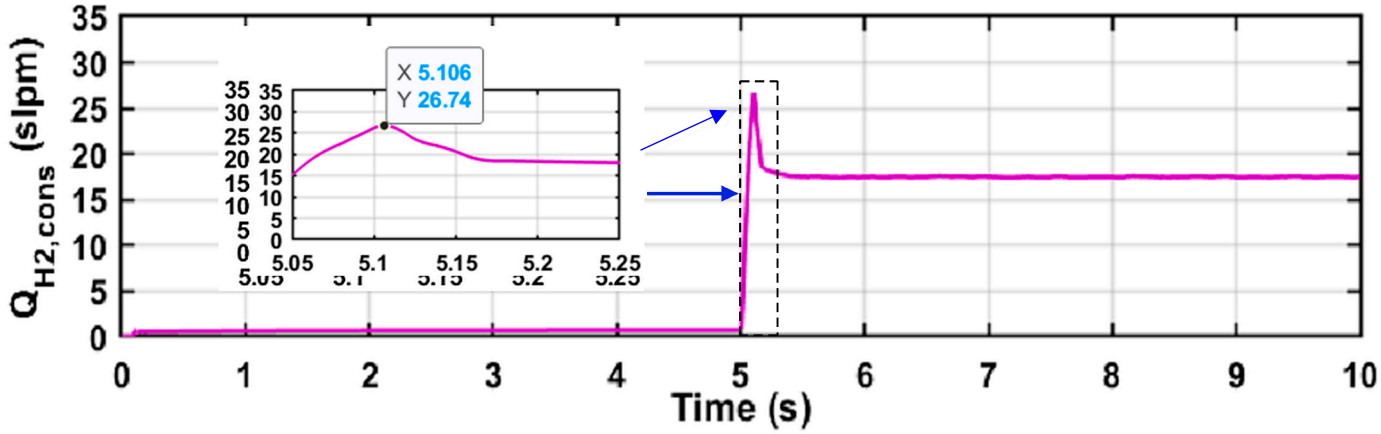


(**a**) DC-DC converter output voltage with NNC

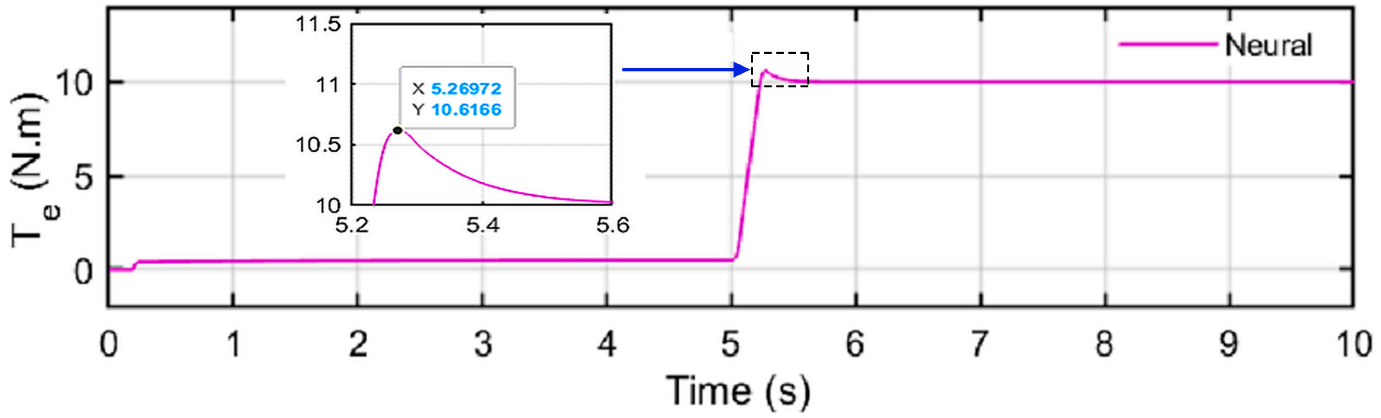


(**b**) ITAE of DC-DC converter output voltage with NNC

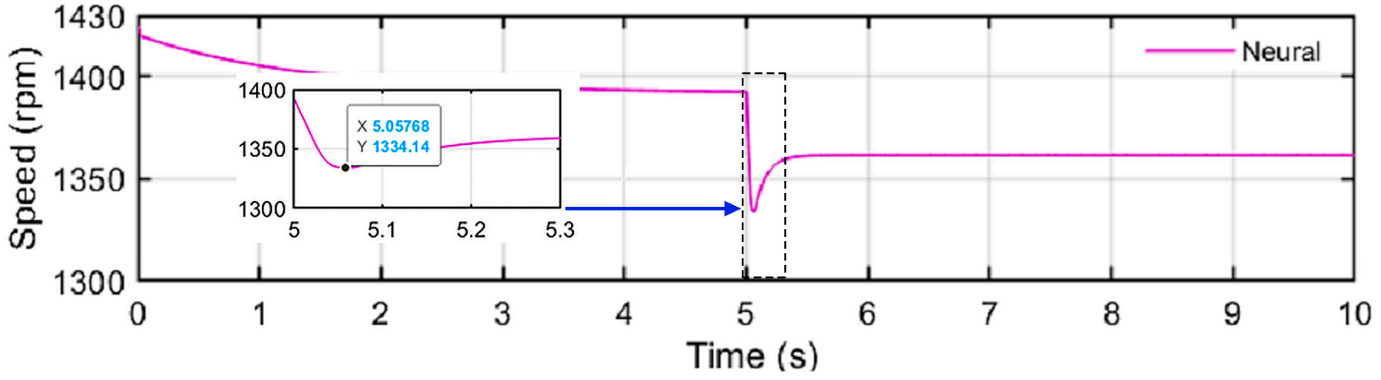
Figure 18. Simulation results of the DC–DC converter controlled by NNC: (**a**) output voltage and (**b**) ITAE.



(**a**) Hydrogen Consumption



(**b**) Motor electromagnetic torque



(**c**) Motor speed

Figure 19. The simulation results based on the NNC for the boost converter controller: (**a**) hydrogen consumption; (**b**) induction motor electromagnetic torque; (**c**) induction motor speed.

As illustrated in Figure 19a–c, the NNC-based system reaches steady-state operation more rapidly than the PI-controlled system with small transient deviations. After the load step, the speed returns to its final value after 0.4 s with the DIOA-tuned PI controller, 0.5 s with the PSO-tuned PI controller (Figure 17d), and 0.2 s with the NNC (Figure 19c).

During the transient interval, the hydrogen consumption reaches a peak of approximately 26.74 slpm, while the motor torque and speed attain maximum and minimum values of about 10.6 N·m and 1334 rpm, respectively. These results indicate improved transient performance compared with the optimally tuned PI controller.

6. Conclusions

The results indicate that adjusting the motor voltage via the DC–DC converter in accordance with load torque variations can reduce hydrogen consumption in a PEMFC-fed three-phase induction motor drive. The DIOA was applied to optimize both the converter reference voltage and the PI controller parameters. The voltage obtained using the DIOA showed a very close agreement with the PSO results, with a deviation of less than 1.1% and a difference in hydrogen consumption of less than 0.02%, and a direct voltage sweep at 2 and 6.5 N·m confirmed the optimum.

Unlike a fixed reference of 537 V, the optimized voltage was adapted to the load, decreasing to 132.76 V at 0.5 N.m load torque (5% full load) and 258.78 V at 2 N.m (20% full load). This adaptive control led to hydrogen savings of 64.65% and 24.17%, respectively. As the load increased, the reference voltage gradually rose toward its rated value of 537 V, where the motor already operates near its maximum efficiency and the saving becomes negligible. The reduction in hydrogen consumption is mainly attributed to improved motor efficiency, particularly under light-load conditions, where efficiency increased from 30.9% to 75.7% at 0.5 N·m.

The dynamic performance of the proposed NNC was tested against the PSO and DIOA methods by introducing a step-load shift from 5% to full load. Under these conditions, the NNC provided the most stable response. It successfully restricted the speed drop to 1334.14 rpm within just 0.057 s and fully recovered to a steady state in about 0.2 s. In contrast, the PI controllers tuned by the DIOA and PSO showed larger deviations, allowing the speed to drop deeper to 1320 rpm and 1313 rpm, respectively. They also reacted slower, taking 0.084 and 0.089 s to reach their minimum speeds, and required much longer recovery times of 0.4 and 0.5 s to restabilize. Finally, the NNC provided better resource management, bringing the hydrogen consumption overshoot down to 26.74 slpm from an initial 28.88 slpm.

These results prove that the neural approach is significantly faster and more robust at handling sudden system changes.

This study is based on simulation only. The model neglects the compressor and auxiliary power, the parasitic losses of the converters (ideal converters are assumed), and the gas-supply dynamics, pressure oscillations, and water transport of the PEMFC. The load torque is assumed to be known to the optimization. Experimental or hardware-in-the-loop validation, the robustness to motor and stack parameter variations, and the simultaneous optimization of voltage and frequency are left for future work.

Author Contributions: Conceptualization, M.M.E., A.E.-S., H.A. and M.A.M.; methodology, M.M.E., A.E.-S., H.A. and M.A.M.; software, M.M.E., A.E.-S., H.A. and M.A.M.; validation, M.M.E., A.E.-S., H.A. and M.A.M.; formal analysis, M.M.E., A.E.-S., H.A., M.J. and M.A.M.; investigation, M.M.E., A.E.-S., H.A., M.J. and M.A.M.; resources, M.M.E., A.E.-S., H.A., M.J. and M.A.M.; data curation, M.M.E., A.E.-S., H.A. and M.A.M.; writing—original draft preparation, M.M.E., A.E.-S., H.A. and M.A.M.; writing—review and editing, M.M.E., A.E.-S., H.A., M.J. and M.A.M.; visualization, M.M.E., A.E.-S., H.A. and M.A.M.; supervision, M.M.E., A.E.-S., H.A. and M.A.M.; project administration, M.M.E.; funding acquisition, M.M.E. and M.J. All authors have read and agreed to the published version of the manuscript.

Funding: The research leading to these results has received funding from the Research and Innovation Authority (RIA) of the Sultanate of Oman under the Block Funding Program, Agreement No. MoHERI/BFP/ASU/GRG/EI/25/173.

Data Availability Statement: The data presented in this study are available on request from the corresponding author.

Conflicts of Interest: The authors declare no conflicts of interest.

References

1. Khan, S.H. Energy storage systems for deep decarbonization: A critical review. *J. Energy Storage* **2026**, *150*, 120485. [CrossRef]
2. Ghazal, M.; Osman, M.; Alhalabi, M.; Gad, A.; Yaghi, M.; Ramadan, M.; Alkhedher, M. Advancements and challenges in green hydrogen production, storage, transportation, and utilization for climate-resilient energy systems. *Results Eng.* **2026**, *29*, 108993. [CrossRef]
3. Li, Y.; Shafique, M.; Luo, X. Hydrogen applications in buildings: A systematic review of decarbonization pathways. *Appl. Energy* **2025**, *405*, 127201. [CrossRef]
4. Owji, A.; Niknam, T.; Taghavi, A.; Pourbehzadi, M. Hydrogen vehicles in the green energy transition: A systematic review of internal combustion engine and fuel cell technologies, energy system integration, and AI application. *Energy Strategy Rev.* **2026**, *64*, 102183. [CrossRef]
5. Vallejo-Cervantes, C.; Espinoza-Andaluz, M.; Iranzo, A. Technical review of commercial LT-PEMFC technologies: Performance, applications and challenges. *Int. J. Hydrogen Energy* **2025**, *176*, 151480. [CrossRef]
6. George, S.; Sehgal, N.; Rana, K.; Kumar, V. A comprehensive review on modelling and maximum power point tracking of PEMFC. *Clean. Energy Syst.* **2022**, *3*, 100031. [CrossRef]
7. Ashraf, H.; Abdellatif, S.O.; Elkholy, M.M.; El-Fergany, A.A. Performance analysis of PEM fuel cells via Puma optimizer with the aid of practical verifications. *Neural Comput. Appl.* **2025**, *37*, 24051–24074. [CrossRef]
8. Ashraf, H.; Abdellatif, S.O.; Elkholy, M.M.; El-Fergany, A.A. Computational Techniques Based on Artificial Intelligence for Extracting Optimal Parameters of PEMFCs: Survey and Insights. *Arch. Comput. Methods Eng.* **2022**, *29*, 3943–3972. [CrossRef]
9. Reddy, A.K.V.K.; Narayana, K.V.L. Meta-heuristics optimization in electric vehicles -an extensive review. *Renew. Sustain. Energy Rev.* **2022**, *160*, 112285. [CrossRef]
10. Min, H.; Wu, H.; Zhao, H.; Sun, W.; Yu, Y. Research on energy management strategy for fuel cell hybrid electric vehicles based on multi-scale information fusion. *Appl. Energy* **2024**, *368*, 123486. [CrossRef]
11. Zhao, X.; Wang, L.; Zhou, Y.; Pan, B.; Wang, R.; Wang, L.; Yan, X. Energy management strategies for fuel cell hybrid electric vehicles: Classification, comparison, and outlook. *Energy Convers. Manag.* **2022**, *270*, 116179. [CrossRef]
12. Luo, Y.; Wu, Y.; Li, B.; Qu, J.; Feng, S.; Chu, P.K. Optimization and cutting-edge design of fuel-cell hybrid electric vehicles. *Int. J. Energy Res.* **2021**, *45*, 18392–18423. [CrossRef]
13. Routh, A.; Ghosh, S.; Dey, I.; Rahaman, M.; Ghosh, A. Optimization of PEMFC pressure control using fractional PI/D controller with non-integer order: Design and experimental evaluation. *Eng. Res. Express* **2024**, *6*, 025001. [CrossRef]
14. Oubelaid, A.; Taib, N.; Nikolovski, S.; Alharbi, T.E.A.; Rekioua, T.; Flah, A.; Ghoneim, S.S.M. Intelligent Speed Control and Performance Investigation of a Vector Controlled Electric Vehicle Considering Driving Cycles. *Electronics* **2022**, *11*, 1925. [CrossRef]
15. Alsofyani, I.M.; Idris, N.R.N.; Lee, K.-B. Dynamic Hysteresis Torque Band for Improving the Performance of Lookup-Table-Based DTC of Induction Machines. *IEEE Trans. Power Electron.* **2017**, *33*, 7959–7970. [CrossRef]
16. Tarusan, S.A.A.; Jidin, A.; Jamil, M.L.M. The optimization of torque ripple reduction by using DTC-multilevel inverter. *ISA Trans.* **2022**, *121*, 365–379. [CrossRef] [PubMed]
17. Moati, Y.; Kouzi, K.; Iqbal, A. Adaptive optimized DTC-SVM using metaheuristic Bat algorithm for DSIM fed by IMC based on robust synergetic speed controller. *Int. Trans. Electr. Energy Syst.* **2020**, *31*, e12697. [CrossRef]
18. Ashraf, H.; Elkholy, M.M.; Abdellatif, S.O.; El-Fergany, A.A. Optimal Starting of IM Energized by PEM Fuel Cells Stack without Energy Storage Devices. In Proceedings of the 2023 24th International Middle East Power System Conference (MEPCON), Mansoura, Egypt, 19–21 December 2023; pp. 1–6.
19. Kakouche, K.; Rekioua, T.; Mezani, S.; Oubelaid, A.; Rekioua, D.; Blazek, V.; Prokop, L.; Misak, S.; Bajaj, M.; Ghoneim, S.S.M. Model Predictive Direct Torque Control and Fuzzy Logic Energy Management for Multi Power Source Electric Vehicles. *Sensors* **2022**, *22*, 5669. [CrossRef] [PubMed]
20. Soumeur, M.A.; Gasbaoui, B.; Abdelkhalek, O.; Ghouili, J.; Toumi, T.; Chakar, A. Comparative study of energy management strategies for hybrid proton exchange membrane fuel cell four wheel drive electric vehicle. *J. Power Sources* **2020**, *462*, 228167. [CrossRef]
21. Raj, A.; Lekhaj, P. An ANFIS based MPPT controller for fuel cell powered induction motor drive. In Proceedings of the 2018 International Conference on Smart Grid and Clean Energy Technologies (ICSGCE), Kajang, Malaysia, 29–31 May 2018; pp. 201–205.
22. Karthikeyan, B.; Sundararaju, K.; Palanisamy, R. ANN-Based MPPT Controller for PEM Fuel Cell Energized Interleaved Resonant PWM High Step Up DC-DC Converter with SVPWM Inverter Fed Induction Motor Drive. *Iran. J. Sci. Technol. Trans. Electr. Eng.* **2021**, *45*, 861–877. [CrossRef]
23. Furuya, T.; Kondo, K.; Yamamoto, T. Experimental study on a PEMFC fed railway vehicle motor drive system. In Proceedings of the Conference Record of the 2006 IEEE Industry Applications Conference Forty-First IAS Annual Meeting, Tampa, FL, USA, 8–12 October 2006; Volume 3, pp. 1249–1252.
24. Pachauri, R.K.; Chauhan, Y.K. Fuzzy logic controlled MPPT assisted PV-FC power generation for motor driven water pumping system. In Proceedings of the 2014 IEEE Students' Conference on Electrical, Electronics and Computer Science, Bhopal, India, 1–2 March 2014; pp. 1–6.

25. Safsouf, K.; Sawma, J.; Kanaan, H.Y. Optimizing the efficiency of a fuel cell–Supercapacitor fed open-end winding induction motor. In Proceedings of the 2024 4th International Conference on Smart Grid and Renewable Energy (SGRE), Doha, Qatar, 8–10 January 2024; pp. 1–6.
26. Herlambang, Y.D.; Apriandi, N.; Prasetyo, T.; Prayitno; Su'udy, A.H.; Sulistiyo, W.; Margana; Marliyati; Sandi, D.K.; Lastomo; et al. Proton Exchange Membrane Fuel Cells (PEMFC)-Based Electric Vehicle: Experimental Analysis of Fuel Flow Rates Effects of Hydrogen Refueling: Proton Exchange Membrane Fuel Cells. *Int. J. Automot. Technol.* **2025**, *27*, 103–110. [CrossRef]
27. Pachauri, R.K.; Chauhan, Y.K. Study and performances analysis of fuel cell assisted vector control variable speed drive system used for electric vehicles. *Int. J. Sustain. Energy* **2017**, *36*, 167–191. [CrossRef]
28. Hamidia, F.; Abbadi, A. SOFC-PV system with storage battery based on cuckoo search algorithm. *Nonlinear Dyn. Syst. Theory* **2022**, *22*, 367–378.
29. Salunke, M.; Hunashikatti, A. Fuel Cell-Inverter System Design for Induction Motor Drives: A Solid Oxide Approach. In Proceedings of the 2024 International Conference on Innovation and Novelty in Engineering and Technology (INNOVA), Vijayapura, India, 20–21 December 2024; Volume 1, pp. 1–6.
30. Jahan, I.; Farrok, O.; Das, N.; Islam, A. Comparative Analysis of Highly Efficient Alkaline Fuel Cell Electric Vehicles. In Proceedings of the 2024 International Conference on Sustainable Technology and Engineering (i-COSTE), Perth, Australia, 18–20 December 2024; pp. 1–6.
31. Khelifi, B.; Ben Salem, F.; Zdiri, M.A.; Abdallah, H.H. A Stand-Alone PV-PEMFC System based SM-ANN-MPPT Controller: Solar Pumping Application using PMSM. *Int. J. Renew. Energy Res.* **2021**, *11*, 662–672. [CrossRef]
32. El-Hay, E.A.; El-Hameed, M.A.; El-Fergany, A.A. Improved performance of PEM fuel cells stack feeding switched reluctance motor using multi-objective dragonfly optimizer. *Neural Comput. Appl.* **2019**, *31*, 6909–6924. [CrossRef]
33. Kusko, A.; Galler, D. Control means for minimization of losses in AC and DC motor drives. *IEEE Trans. Ind. Appl.* **1983**, *IA-19*, 561–570. [CrossRef]
34. Kirschen, D.S.; Novotny, D.W.; Lipo, T.A. On-Line Efficiency Optimization of a Variable Frequency Induction Motor Drive. *IEEE Trans. Ind. Appl.* **1985**, *IA-21*, 610–616. [CrossRef]
35. Kioskeridis, I.; Margaris, N. Loss minimization in scalar-controlled induction motor drives with search controllers. *IEEE Trans. Power Electron.* **1996**, *11*, 213–220. [CrossRef]
36. Abrahamsen, F.; Blaabjerg, F.; Pedersen, J.; Grabowski, P.; Thogersen, P. On the energy optimized control of standard and high-efficiency induction motors in CT and HVAC applications. *IEEE Trans. Ind. Appl.* **1998**, *34*, 822–831. [CrossRef]
37. Sousa, G.C.D.; Bose, B.K.; Cleland, J.G. Fuzzy logic based on-line efficiency optimization control of an indirect vector-controlled induction motor drive. *IEEE Trans. Ind. Electron.* **1995**, *42*, 192–198. [CrossRef]
38. Liu, Z.; Zhao, J.; Qin, Y.; Wang, G.; Shi, Q.; Wu, J.; Yang, H. Real time power management strategy for fuel cell hybrid electric bus based on Lyapunov stability theorem. *Int. J. Hydrogen Energy* **2022**, *47*, 36216–36231. [CrossRef]
39. Pukrushpan, J.T.; Stefanopoulou, A.G.; Peng, H. *Control of Fuel Cell Power Systems*; Springer: London, UK, 2004.
40. Alavi, O.; Rajabloo, T.; De Ceuninck, W.; Daenen, M. Non-Isolated DC-DC Converters in Fuel Cell Applications: Thermal Analysis and Reliability Comparison. *Appl. Sci.* **2022**, *12*, 5026. [CrossRef]
41. Ashraf, H.; Elkholy, M.M.; Abdellatif, S.O.; El-Fergany, A.A. Synergy of neuro-fuzzy controller and tuna swarm algorithm for maximizing the overall efficiency of PEM fuel cells stack including dynamic performance. *Energy Convers. Manag. X* **2022**, *16*, 100301. [CrossRef]
42. Ram, V.; Infantraj; Salkuti, S.R. Modelling and Simulation of a Hydrogen-Based Hybrid Energy Storage System with a Switching Algorithm. *World Electr. Veh. J.* **2022**, *13*, 188. [CrossRef]
43. Elkholy, M.M.; Elhameed, M.A. Minimization of Starting Energy Loss of Three Phase Induction Motors based on Particle Swarm Optimization and Neuro Fuzzy Network. *Int. J. Power Electron. Drive Syst. (IJPEDS)* **2016**, *7*, 1038–1048. [CrossRef]
44. Zhang, Y.; Xia, B.; Yang, H.; Rodriguez, J. Overview of model predictive control for induction motor drives. *Chin. J. Electr. Eng.* **2016**, *2*, 62–76. [CrossRef]
45. Hossen, M.B.; Habibullah, M. Robust model-free predictive torque control for induction motor drive based on an ultralocal model. *IEEE Access* **2025**, *13*, 47514–47524. [CrossRef]
46. El Romeh, A.; Snášel, V.; Mirjalili, S. Dholes-inspired optimization (DIO): A nature-inspired algorithm for engineering optimization problems. *Clust. Comput.* **2025**, *28*, 853. [CrossRef]

Disclaimer/Publisher's Note: The statements, opinions and data contained in all publications are solely those of the individual author(s) and contributor(s) and not of MDPI and/or the editor(s). MDPI and/or the editor(s) disclaim responsibility for any injury to people or property resulting from any ideas, methods, instructions or products referred to in the content.